Eidgenössische Technische Hochschule Zürich
Swiss Federal Institute of Technology Zurich

Trapped Ion Quantum Information

ETH Zürich, Department of Physics

Coherent Control Laser System for the Quantum State Manipulation of Trapped Ions

Master Thesis

Supervisor:
Prof. Dr. Jonathan Home

Student:
Karin Fisher

Spring Semester 2013

Abstract

This thesis documents the design and implementation of a system that is used to perform coherent state manipulations on $^{40}Ca^{+}$. Two contributions are discussed: first, the design for the water cooling and interlock system for the high current field coils, and second, the setup of the laser system at 729 nm. The laser system consists of three independently frequency tunable beams, two for ion state control and one for the cancellation of the AC Stark shift, which are focused onto the ion. The linewidth of the laser is narrowed by using a high-finesse cavity. A scheme for fiber-noise cancellation is proposed and partially implemented, and will be used to further narrow the linewidth of the laser. Lastly, data from preliminary measurements is presented. This includes quantum jumps, Ca^{+} spectroscopy, and the observation of Rabi oscillations.

Acknowledgements

Firstly, thank you to Professor Jonathan Home for giving me the opportunity to work in the TIQI lab, and also for being the most involved professor I've ever worked with. For showing me helpful techniques in the lab and explaining both the simple and the more complex, I am extremely grateful.

Thank you to Daniel Kienzler for supervising me and always taking time to show and explain all of the aspects of the project and beyond. To Hsiang-Yu Lo for contributing some of your magic optics skills by helping me choose lenses and helping me to couple my beam into the trap. I probably would have been trying for many more hours otherwise. To Vlad Negnevitsky and Dr. Ben Keitch for your help especially with debugging my circuit as well as providing amusing banter in the office. To Frieder Lindenfelser for helping me to construct AOM drivers and making sure that I would have enough amplifiers. To Ludwig de Clercq for being there and supporting me even when I was more stressed out than I needed to be, and proofreading my thesis even though you didn't have to. To Florian Leupold, Dr. Joseba Alonso, and Matteo Fadel for generally making my experience better, whether at lunch or during a game of kicker.

Also, thank you to the stabhochspringerinnen and stabhochspringern (and Marco) of the LCZ for keeping me sane, putting up with me, and keeping me happy. Also specifically to Anja for reminding me that I should be working on my thesis while in South Africa... And thank you to Lauren Kuntz and Patrick Barragán for proofreading and for being there for me always.

In general, thank you to everyone in the lab for making this by far my best ever lab experience. I nearly left Zürich before starting my thesis because I was so burned out and homesick. Now I don't want to leave. You have all helped me become excited about research again.

Contents

1 Introduction

Recently there has been a large focus in physics towards quantum computing and the manipulation of quantum bits (qubits). Ion trapping is one of the leading fields working towards quantum information processing (QIP). Trapped ions are relatively easy to manipulate using lasers and can have long coherence times, and thus offer an attractive choice for a qubit. [1]

To trap an ion, one needs to create a potential well in which the ion sits. One method for trapping an ion is using a Paul trap, which uses DC and RF fields to create the well. For more information about Paul traps, see [2].

A harmonically trapped ion has both internal electronic states and vibrational states. A coherent light source tuned near resonance with an internal transition can interact with both types of states. For a qubit, the internal transition is chosen such that it can be described as a two level system with states $|\downarrow\rangle$ and $|\uparrow\rangle$.

The Hamiltonian describing the interaction of light with a trapped ion is given by

$$\hat{H} = \hat{H}_o + \hat{H}_i \tag{1}$$

$\hat{H}_o$ describes the state of the ion (motional and internal), while $\hat{H}_i$ describes the interaction between the ion and the light field. Under the rotating wave approximation and in the interaction picture, $\hat{H}_i$ is transformed into $\hat{H}_I$ and takes the form

$$\hat{H}_I = \frac{\hbar}{2}\Omega(e^{i\eta(\hat{a}_I+\hat{a}_I^\dagger)}\hat{\sigma}^+ e^{-i\Delta t} + e^{-i\eta(\hat{a}_I+\hat{a}_I^\dagger)}\hat{\sigma}^- e^{i\Delta t}) \tag{2}$$

where Δ is the difference between the laser frequency and the transition frequency, $\hat{a}_I = \hat{a}e^{-i\omega_t t}$, and

$$\eta = k\sqrt{\frac{\hbar}{2m\omega_t}}\cos(\theta) \tag{3}$$

is the Lamb Dicke parameter, k is the wavenumber, and ω_t is the trap frequency, and θ is the incidence angle of the light with respect to the trap axis. The Lamb Dicke parameter describes the extent of the ground state wavefunction of the oscillator. [3]

In the Lamb Dicke regime, where the extent of the wavepacket is much smaller than the wavelength of light, the exponentials in $\hat{H}_I$ can be expanded to the lowest order in η. The resulting interaction Hamiltonian is given by

$$\hat{H}_I = \frac{\hbar}{2}\Omega((1 + i\eta(\hat{a}e^{-iw_t t} + \hat{a}^\dagger e^{iw_t t})\hat{\sigma}^+ e^{-i\Delta t}) + (1 - i\eta(\hat{a}e^{-iw_t t} + \hat{a}^\dagger e^{iw_t t})\hat{\sigma}^- e^{i\Delta t})) \tag{4}$$

The light couples to a carrier transition and two sidebands. When $\Delta = 0$, the carrier transition is resonantly excited, and the Hamiltonian can be approximated by

$$\hat{H}_I = \frac{\hbar}{2}\Omega(\hat{\sigma}^+ + \hat{\sigma}^-) \tag{5}$$

When $\Delta = \pm\omega_t$, the red or blue sideband is resonantly excited. The Hamiltonian for the red sideband can be approximated by

$$\hat{H}_I = i\frac{\hbar}{2}\eta\Omega(\hat{a}\hat{\sigma}^+ - \hat{a}^\dagger\hat{\sigma}^-) \tag{6}$$

and the Hamiltonian for the blue sideband by

$$\hat{H}_I = i\frac{\hbar}{2}\eta\Omega(\hat{a}^\dagger\hat{\sigma}^+ - \hat{a}\hat{\sigma}^-) \tag{7}$$

The carrier transition couples $|\downarrow, n\rangle$ with $|\uparrow, n\rangle$, where n is the number of vibrational quanta. The red sideband couples $|\downarrow, n\rangle$ with $|\uparrow, n-1\rangle$, whereas the blue sideband couples $|\downarrow, n\rangle$ with $|\uparrow, n+1\rangle$. [4]

The coupling of motional and internal states allows for operations such as sideband cooling (see [5]) and the implementation of quantum gates. An example of such a gate is briefly discussed in Section 1.2.

1.1 Calcium Ion

In the TIQI lab at ETH Zürich, the ion on which we will perform coherent manipulations is $^{40}Ca^+$. Its internal level structure is shown in Figure 1. A good transition for coherent manipulations is the quadrupole transition between $4^2S_{1/2}$ and $3^2D_{5/2}$ because it has a long lifetime of 1.1 seconds. [6] When placed in a magnetic field, the $S_{1/2}$ state splits into two levels and the $D_{5/2}$ state splits into six states as according to the Zeeman effect. We use a field strength of 119.64 G. We have chosen this field because we would like to trap beryllium as well as calcium in the future. For $^9Be^+$, at this field, small changes in the magnetic field will not, to first order, affect the transition in Be^+ used for quantum manipulation.

For our Ca^+ qubit, we will address the $4^2S_{1/2}$ $m = 1/2$ to $3^2D_{5/2}$ $m = 3/2$ transition. This transition has a frequency of 411042.263 GHz, which corresponds to a wavelength of approximately 729 nm. The 729 nm transition will also be used for sideband cooling.

Another aspect of the 729 nm transition is that for a $|\Delta m| = 1$ transition, if the beam is parallel to the magnetic field, then the coupling strength is not dependent on the polarization of the light. Under the same conditions, the coupling strengths of the $|\Delta m| = 0$ and $|\Delta m| = 2$ transitions are low compared to the strength of the $|\Delta m| = 1$ transition. A diagram of the coupling strengths, taken from [4], is shown in Figure 2. This geometry is a good choice since the low coupling strength to nearby m states reduces the Stark shift due to off-resonant coupling, as discussed in Section 1.3. This geometry is also convenient for practical considerations, since we need not worry about the polarization of the incoming light. [4]

The other transitions are important as well, though they are less relevant to this thesis. The 397 nm transition is used for Doppler cooling and state detection. If the ion falls into the $3^2D_{3/2}$ state, a laser at 866 nm is used for repumping. The 854 nm transition is used to reset the state after being shelved in the $3^2D_{5/2}$ state.

The aim of this thesis was to create a system capable of coherently addressing the 729 nm transition. This manifested in two ways: setting up the field coils such that they could be safely operated, and setting up the 729 nm laser system.

Two main things had to be accomplished for the safe operation of the field coils at this field. The first was setting up the water cooling of the coils, which is discussed in Section 2.2. The second was setting up an emergency shutoff for the coil system, which is discussed in Section 2.3.

For the laser system, we needed a system that could address the 729 nm transition and motional sidebands. This required directing three beams of specific frequencies at the ion: two beams for coherent manipulation–the ion control beams–and one beam to counteract the AC Stark shift. The motivation behind these 3 beams is given in the following sections.

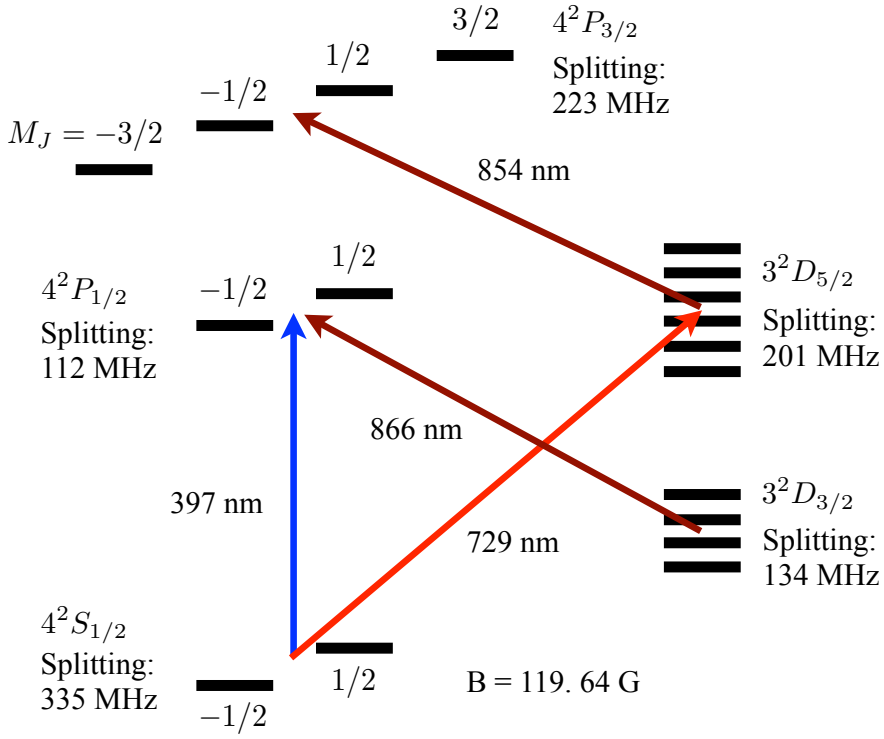

Figure 1: Transitions for $^{40}Ca^+$ along with their wavelengths and splittings at 119.64 G.

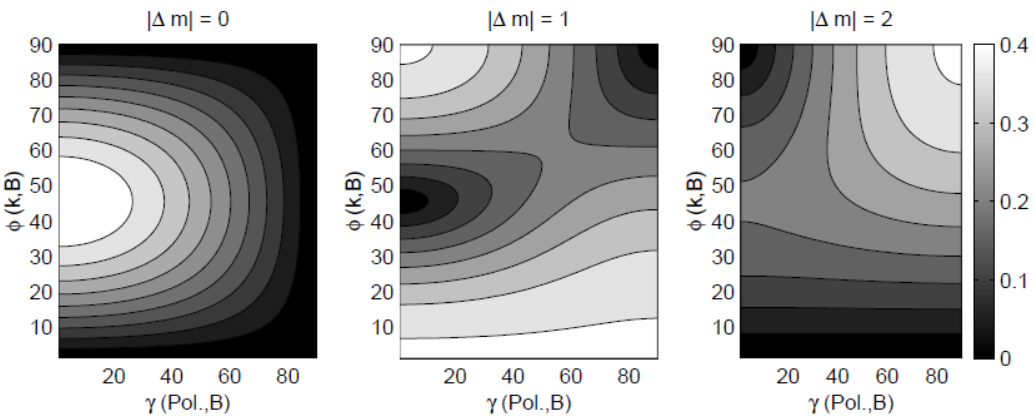

Figure 2: Coupling strengths of the transitions between different m states of the $S_{1/2}$ to $D_{5/2}$ transition. ϕ is the angle between the magnetic field and the laser beam, and γ is the angle between the polarization and the magnetic field vector. Regions of light color are high coupling strength, whereas regions of dark area are low coupling strength. From [4].

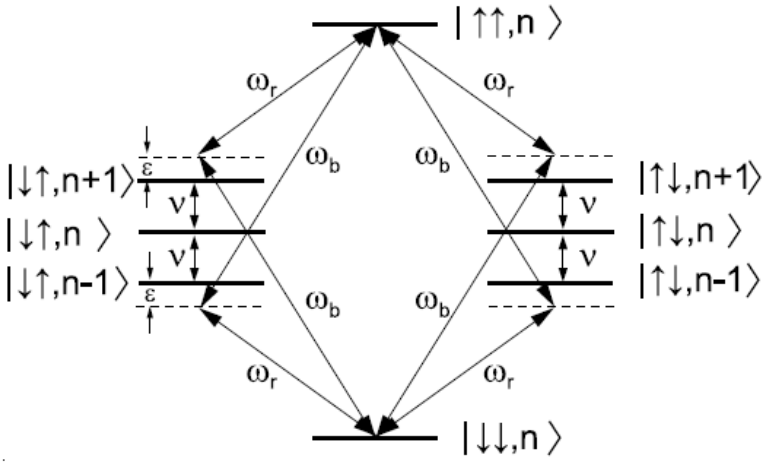

Figure 3: Diagram showing the Mølmer Sørensen gate. From [7]. The upper and lower sidebands are addressed, coupling states $|\uparrow\uparrow\rangle$ and $|\downarrow\downarrow\rangle$.

1.2 Quantum Gates

In order to implement quantum gates, one must be able to coherently address the motional sidebands of the 729 nm transition. One example of a gate we may want to implement is a Mølmer-Sørensen gate. The Mølmer-Sørensen gate entangles two ions by exciting the transition with beams tuned close to the upper and lower motional sidebands. Because the beams are tuned near both the upper and lower sidebands, the motional state in the $|\downarrow\downarrow\rangle$ to $|\uparrow\uparrow\rangle$ transition is unchanged. This transition can, however, take different paths, thereby creating an entangled state due to the interference of the paths. A diagram of this interaction is given in Figure 3. A complete quantum mechanical description of the gate is given in [7] and in [8]. This is only one example where we would want two coherent beams tuned close to the 729 nm transition.

1.3 AC Stark Shift

When a transition is excited by far detuned light, a shift in the energy levels involved in the transition will occur. This shift is called the AC Stark shift. Light is considered far detuned when $\Delta \ll \Omega_R$, where Δ is the detuning between the light and the transition frequency, and Ω_R is the Rabi frequency of the transition. [9] Perturbation theory shows that the shift of each level is given by

$$\Delta\nu_{Stark} = \pm\frac{\Omega_R^2}{4\Delta} \tag{8}$$

Blue detuned light will cause the energy levels to shift closer together, while red detuned light will cause the transition to shift farther apart. [10]

When quantum manipulations are performed on Ca^+, the AC Stark shift occurs due to several different off-resonant couplings. The Stark shift is a problem when exciting a motional sideband due to the high intensities needed due to the low coupling strength. Exciting a motional sideband will cause off-resonant coupling to the carrier transition. The shift in the energy of the carrier transition will also cause a shift in the energy of the sideband transition. This situation is diagrammed in Figure 4, where $\Delta = \omega_t$, the trapping frequency.

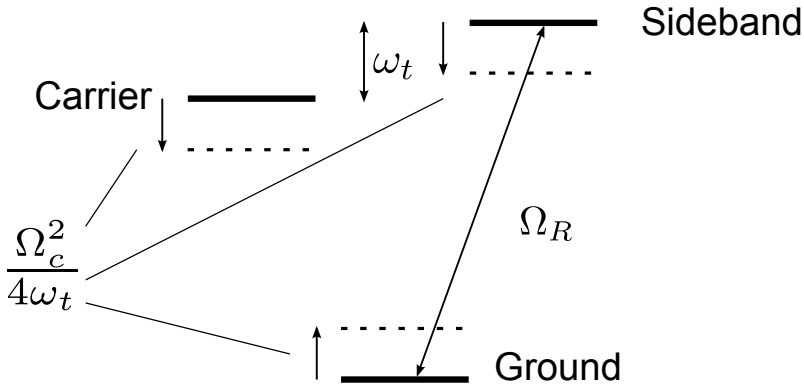

Figure 4: AC Stark shift due to light exciting the sideband transition, off-resonantly coupling to the carrier.

Although coupling to the carrier transition is the dominant contribution to a shift in the sideband transition, it is not the only contribution. Off resonant coupling to other m states as well as coupling to the P states will further contribute to the Stark shift seen in the sideband transition.

The implementation of quantum gates and algorithms relies on the ability to apply precisely tuned laser pulses to excite specific transitions. The presence of a shift will change the effect of a pulse on the state. It is therefore necessary to counteract the AC Stark shift. This can be done by shining in an extra laser beam which causes a Stark shift that exactly cancels the Stark shift due to the control beams. This method has been implemented previously by Häffner et al. at University of Innsbruck. [11] The detuning and intensity of the beam is adjusted such that the overall shift is minimized. The detuning of the Stark beam should be large enough that it does not induce population transfer into the D states. More information about the Stark shift compensation beam can be found in [12], and the exact method for choosing the intensity and detuning of the Stark beam is described in [13].

2 Field Coils

Helmholtz coils are used to achieve the magnetic field needed for the Zeeman splitting of the $^{40}Ca^+$. The trap used is a segmented Paul trap designed by Daniel Kienzler. The trap is placed in the center of the two coils within a vacuum system. A simple diagram of the coil setup is in Figure 5. The red dot indicates the location of the ion.

2.1 Field Characterization

Before inserting the trap between the coils, it was necessary to perform a field characterization of the coils such that we knew at what current to run our coils to get the desired level splitting.

The coils were hooked up in series in a Helmholtz configuration, and a Gauss meter was placed roughly in the middle between the two coils. The current driving the coils was stepped from 0 to 1 A in increments of .05 A, and the voltage and resulting field were recorded. A plot of the data can be found in Figure 6. As is expected, the field strength is linear with respect to current. The linear fit of the data gives the equation

$$\mathrm{B} = (1037.8)\mathrm{I} + .0563 \tag{9}$$

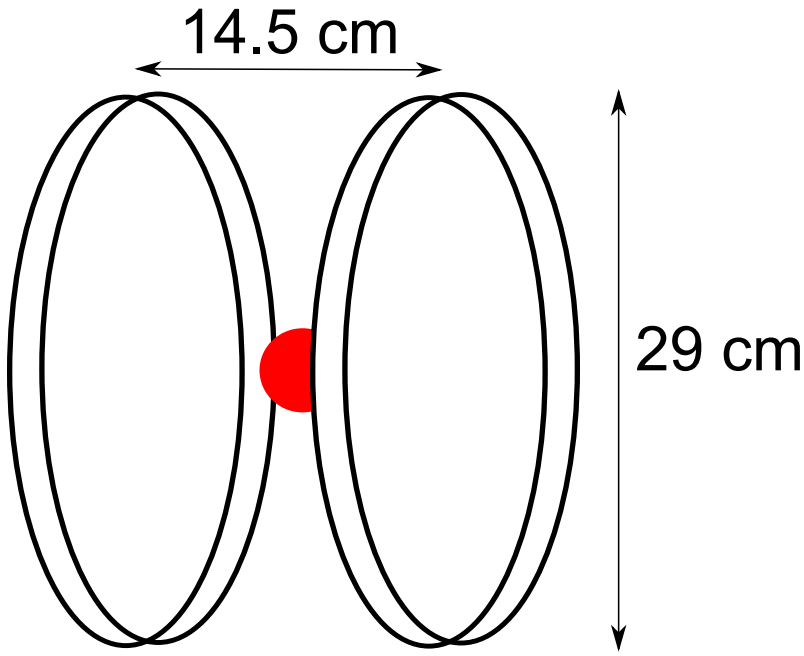

Figure 5: Ion in the center of the field coils. In reality, the ion is trapped in a trap that sits in a vacuum system between the coils.

where B is the magnetic field in mG and I is the current in A.

By extrapolating, we calculate that a field of 120 G occurs at 115.6 A.

The field at the center of the Helmholtz coils can be approximated by

$$\mathrm{B} = (\frac{4}{5})^{3/2} \frac{\mu_o N \mathrm{I}}{r} \tag{10}$$

where N is the number of turns per coil, and r is the radius of the coils. This is an idealized equation. The coils have an inner diameter of 29 cm and an outer radius of 34 cm. There are 19 turns per coil. The calculated slope B/I, using an average diameter of 31.5 cm, is calculated to be 1084.7 mG/A. This is close to the measured slope of 1037.8 mG/A.

2.2 Water Cooling

Because of the high currents being run through the Helmholtz coils, temperature control of the coils is a major concern. The windings are made from hollow copper tubing such that they can be water cooled.

The cooling water is built into the lab facilities. The flow can be turned on or shut off using a solenoid controlled valve. We use a filter to keep the water clean going through the coils, and a pressure regulator to ensure that the flow does not exceed 0.3 l/min. The water is hooked up to the coils in parallel such that the two coils have roughly the same temperature, minimizing the temperature gradients around the trap.

A flow sensor[1] is placed before the return and is used to monitor the flow of water for the interlock system, as described below. A diagram of the water cooling path is shown in Figure 7. The pressure regulator is placed before the filter because the filter is old and we did not want to have too much pressure in it.

[1] Cynergy3 Ultrasonic Flow Meter UF08B

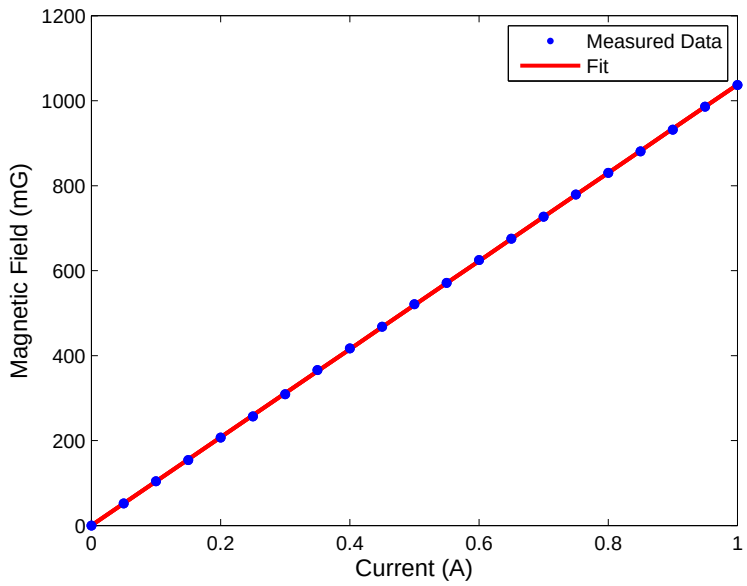

Figure 6: Measurement of magnetic field strength vs. current for the Helmholtz coils.

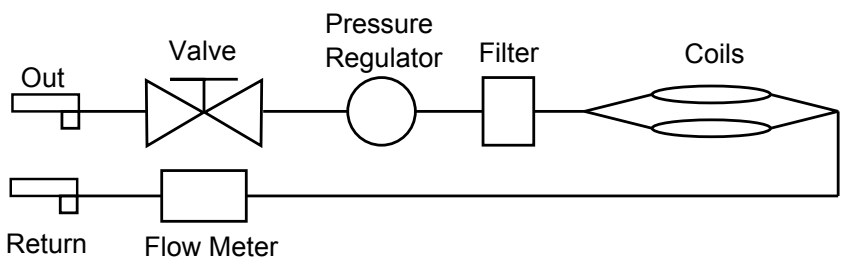

Figure 7: Path taken by cooling water.

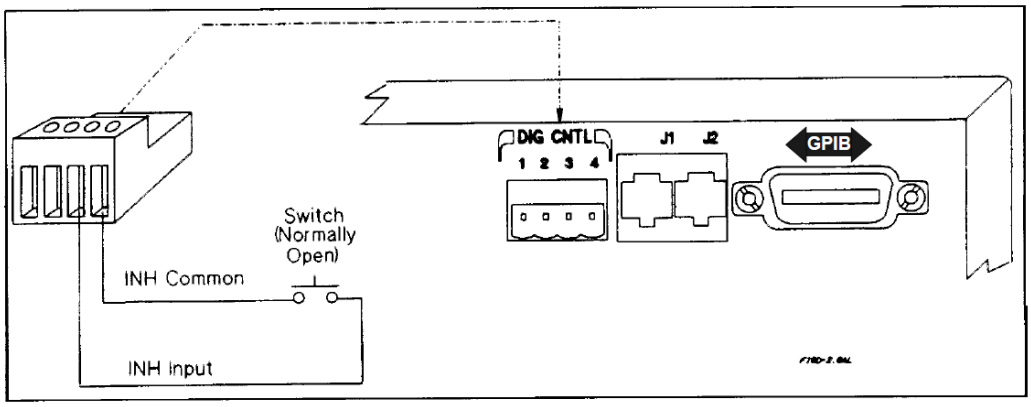

Figure 8: Built-in interlock for the power supply. From [14].

2.3 Interlock

While the water cooling keeps the coils at a safe temperature, it is easy to imagine a situation in which the water cooling might fail, for example, a broken pipe. In this situation, we would run into both the coils overheating and the lab flooding. It is prudent to design a shut off system that protects the lab against this sort of emergency.

The power supply that we are using to power the field coils is an Agilent 6682A. It is able to source up to 240 A at 21 V. The power supply has a built-in interlock system that can be hooked up to an external control. The power supply has a digital connector that when pin 3 is driven low (or shorted to pin 4), the power supply will stop supplying current, as shown in Figure 8. In order to run the power supply once the interlock has been triggered, both the cause for the trigger must be removed, and the fault must be reset on the front panel. This means that once the interlock has been triggered, even if the reason for the fault is removed, a person must physically be present to reset the power supply. In this way, a lab member can check the setup to find the reason for the fault before the power supply will turn on again.

There are two main aspects to this shutoff system. The first monitors the temperature of the coils, and the second monitors the flow of the water cooling. The circuit diagram for the interlock system is given in Appendix A.

2.3.1 Temperature Shutoff

The temperature-controlled shutoff monitors the temperature of the coils and shuts off the power supply controlling the coils if the temperature is too high.

Four points on the coil are monitored with thermistors[2]: the two inflow points and the two outflow points. The thermistors are taped onto the copper, with a layer of electrical tape underneath to prevent electrical contact.

Each thermistor is placed in series with another resistor to create a voltage divider. The voltage drop across each thermistor is compared to an independent adjustable reference voltage using a comparator[3]. When one thermistor temperature rises above its reference temperature, mechanical relay shuts. When the relay shuts, it triggers the power supply's built-in interlock, and the power supply stops sourcing current. The relays for the four sensors are in parallel, which ensures that it takes only one thermistor to overheat for the

[2]Vishay NTCLE203E310GB0
[3]LM339N

supply to shut off. The relays are normally closed, so the power supply cannot source current without the interlock being active.

To set the reference voltage, the coils were run at full current and water cooling for an hour and a half. The reference voltages were adjusted until the shutoff point was passed. Then the reference was set just above this shutoff point.

2.3.2 Flow Shutoff

The second part of the shut off system monitors the flow of the cooling water. The flow sensor placed in the return line of the cooling water monitors the flow rate. When powered, the flow sensor returns a voltage corresponding to the flow rate of the water. This voltage is compared using a comparator to a set point which corresponds to approximately 0.25 l/min.

When the flow is too low, the flow shutoff circuit does two things. First, it closes a solenoid-operated valve at the cooling water output. This is because if there is a block in the cooling, or if a pipe breaks, the flow will drop, and the valve prevents flooding or further damage to the cooling system.

Second, if the flow is low, the coils may not be properly cooled. Therefore, the circuit also is connected to a relay in parallel with the relays for the temperature sensors. If the flow is low, the power supply will shut off.

In order to run the cooling system and run the power supply, there must be flow through the flow sensor. Because the valve is shut when the flow is low, there is a switch that overrides the shutoff circuit and opens the valve (but does not turn on the power supply). It is necessary to open this switch for a few seconds and let the flow sensor register a flow. When the flow is detected, a green LED on the flow sensor will blink. At this point, one must close the switch so that the interlock system is ready to go.

In short, the safety shut off system for the Helmholtz coils monitors two things: the temperature of the coils and the flow rate of the cooling water. When the temperature increases beyond a set point, the power supply is shut down. When the flow drops low, both the cooling water shuts off, and the power supply is shut down.

3 Setup Background

3.1 Double-Passed AOMs

In our setup, we use three acousto-optic modulators (AOMs) in a double-pass configuration. Double-passing an AOM is a method of shifting the frequency of laser light by using an AOM while reducing the effect of frequency changes on beam angle. This configuration also allows for a wider frequency range with the same AOM since the frequency shift is doubled. I will briefly explain the double-pass scheme used in this setup. For more information, see [15].

In a double-pass AOM, the beam first passes through a polarizing beam splitter (PBS) and enters the AOM, where it is diffracted into the ± 1 order. The beam passes through a quarter wave plate. The zeroth order is blocked, and the first order is reflected via a mirror (in a cat's eye configuration) back onto itself. The beam passes back through the quarter wave plate and into the AOM. The beam is diffracted into the first order again, which after emerging from the AOM, overlaps with the incoming beam. The beam is separated from the incoming beam when it passes back through the beamsplitter, since

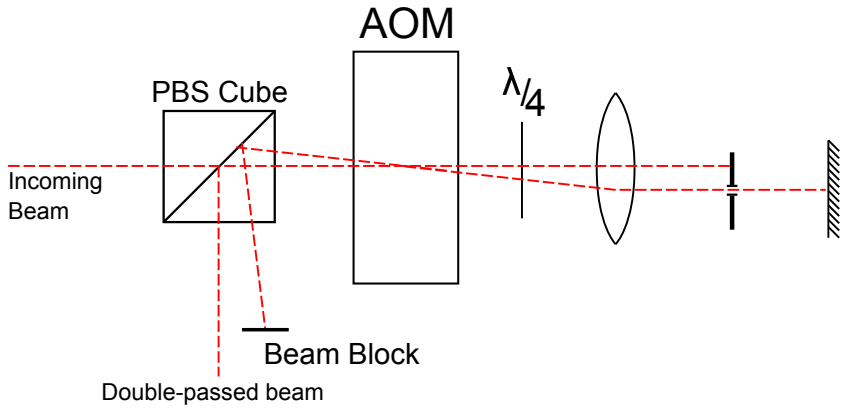

Figure 9: AOM in double-pass configuration.

the double-pass through the quarter wave plate rotates the polarization by 90 degrees. A diagram can be found in Figure 9.

The cat's eye reflector consists of a lens which is placed one focal length away from the AOM and one focal length away from a reflecting mirror. The zeroth and first orders will emerge from the lens parallel to one another, such that changing the frequency of the AOM changes only their spacing. This means that even over a wide range of frequencies, the mirror remains at the correct angle for retro-reflecting the first order back onto itself. As a result, the double-pass diffraction efficiency has a much larger bandwidth.

3.2 Fiber-Noise Cancellation

In order to improve coherence, it is necessary to ensure a narrow laser linewidth. Phase noise in a fiber is one factor that contributes to the broadening of the linewidth. Phase noise becomes a problem in long fibers. A method for fiber-phase-noise cancellation has been pioneered by L.-S. Ma et al. at NIST in Boulder, CO. [16]

The basic idea of fiber-phase-noise-cancellation is to cancel out the effect of phase noise in the fiber by applying exactly the opposite phase variations before the fiber. This method operates under the assumption that the phase noise due to the fiber is slowly varying compared to the bandwidth of the cancellation system. [16]

One method of cancelling out this noise involves using an AOM to apply shifts opposite to what the signal will experience in the fiber. The specific scheme that we employ is modeled on the scheme used by the Ion Storage group at NIST. [17] Other schemes for fiber-noise cancellation are described in [16] and [18]. A diagram of the scheme can be found in Figure 10.

The incoming light can be described by

$$E = E_o \cos(\omega t) \tag{11}$$

where ω is the frequency of the light and E_o is the initial electric field magnitude. This beam is sent through the AOM and is diffracted into the first and zeroth orders, both of which are utilized for the fiber-noise cancellation. The first order diffraction is shifted by Δ by the AOM, yielding now

$$E = E_o \cos((\omega + \Delta)t - \phi_{AOM}) \tag{12}$$

where ϕ_{AOM} is the phase added by the AOM. The beam then travels through the long fiber and acquires a phase of ϕ_f. The light is partially reflected back down the fiber (about

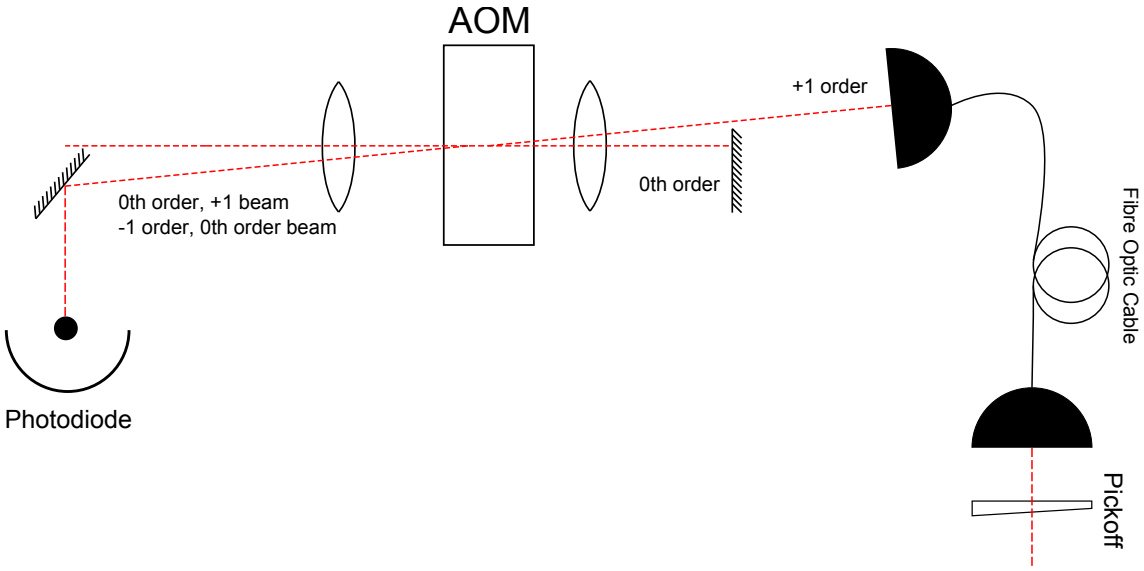

Figure 10: Fiber-noise cancellation setup as inspired by [17]. Incoming light gets diffracted into the first order and is coupled into a fiber. At the end of the fiber, the beam is partially reflected back and double-passed into its zeroth order. The zeroth order is also double-passed, but into the -1 order. The beat between the +1 and -1 orders is picked up by a photodiode and used to feedback into the AOM.

4%) by a glass wedge[4] with an uncoated front face, referred to here as a pickoff. After passing through the fiber twice, the light can be described by

$$E = E_r \cos((\omega + \Delta)t - \phi_{AOM} + 2\phi_f) \tag{13}$$

where E_r is the reduced field magnitude. This signal is sent back through the AOM, where the zeroth order diffraction is picked off by a mirror and sent into a photodiode. The electric field has the same form as above.

The zeroth order diffraction of the original incoming light, on the other hand, is reflected back into the AOM by a mirror. The first order diffraction of the second pass is also picked off by a mirror and sent into a photodiode. This beam is described by

$$E = E_r \cos((\omega - \Delta)t + \phi_{AOM}) \tag{14}$$

The two beams sent into the photodiode are overlapped because they are diffracted into the same beam path by the AOM. These two beams form a beatnote at the frequency

$$\omega_{beat} = 2\Delta t - 2\phi_{AOM} + 2\phi_f \tag{15}$$

By locking ϕ_f to ϕ_{AOM}, one can precancel the phase noise acquired in the fiber. The cancellation is implemented by using feedback to adjust the frequency sent to the AOM.

4 Experimental Setup

There are four main portions of the 729 nm setup: the fiber-noise cancellation setup, the control board, the beam delivery setup, and the high-finesse cavity setup (HFC). The

[4] ThorLabs BSF10-B

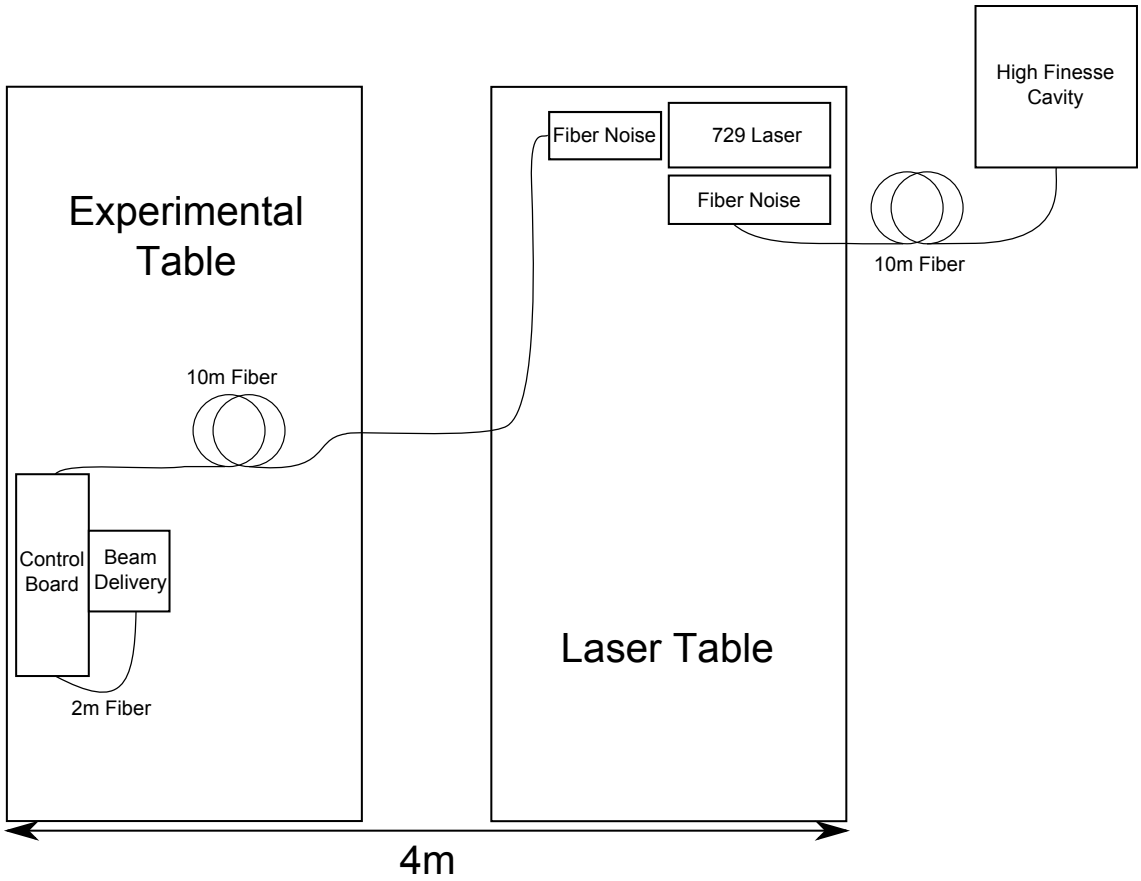

Figure 11: Location of sections of setup around the lab.

fiber-noise cancellation setup has two parts: that which provides the cancellation for the main 729 nm beam (the beam that eventually goes to the ion), and that which provides the cancellation for the beam for laser stabilization. The control board is where the two ion control beams and the Stark beam are created, and the beam delivery board delivers these three beams to the trap. The HFC setup is used for frequency stabilization of the 729 nm laser. In this section, I will first describe how all of the pieces fit together, and then go into detail about each part.

The laser that we are using for the 729 nm beam is a Toptica TA pro. It is a diode laser which is amplified by a tapered amplifier. The laser has two ports: the main laser port, which puts out about 450 mW of light by utilizing a tapered amplifier, and a probe port, which picks off about 3 mW of light from the diode laser before the TA. The main beam is used for ion control, and the probe beam is used for laser stabilization.

The setup is spread over three optical tables. The relevant layout of the tables in the lab can be found in Figure 11. The 729 nm laser is situated on the laser table, whereas the trap is located on the experimental table. The HFC is located to the right of the laser table. More information on the special table created for the HFC can be found in [19].

The main beam travels through the fiber-noise cancellation on the laser table and is then carried to the experimental table by a 10m fiber. At the end of the fiber, the beam enters the control board setup. After passing through the control board setup, the beam is carried by a 2m fiber to the beam delivery board, which subsequently delivers the beam to the trap.

The probe beam, on the other hand, travels through the fiber-noise cancellation before

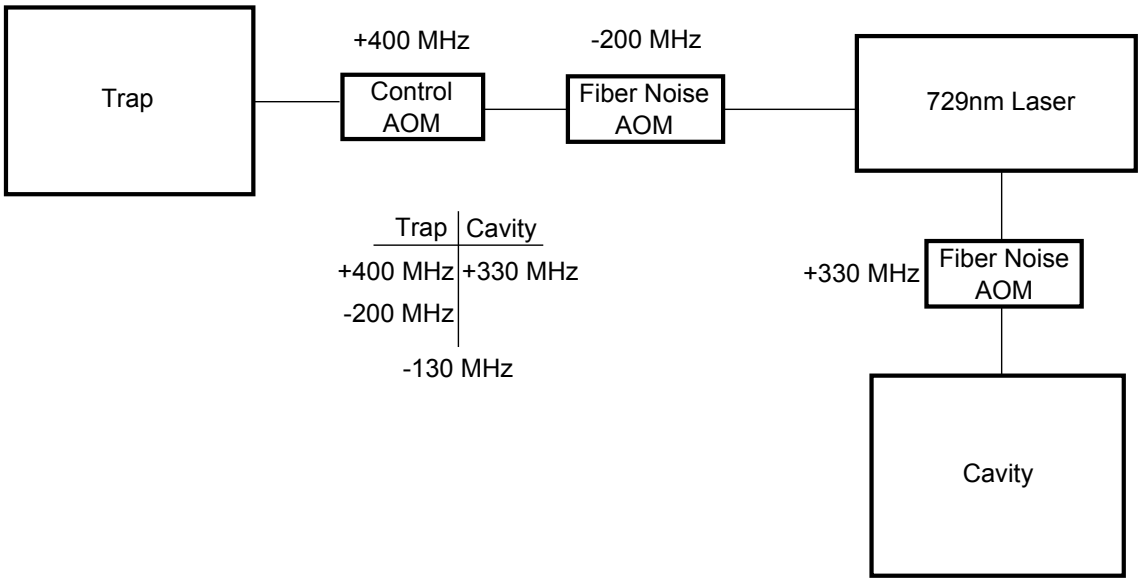

Figure 12: Diagram of AOM frequencies chosen to match cavity frequency with ion transition frequency.

being transmitted to the HFC table by a 10m fiber. All of the fibers used are polarization maintaining[5], and prior to each fiber there is a half-wave plate to align the polarization of light to the axis of the fiber.

4.1 Choice of AOM Frequencies

The $m = +1$ transition from $4^2S_{1/2}$ to $3^2D_{5/2}$ requires a frequency of 411042.263 GHz at 119.64 G. A high-finesse cavity is used to narrow the linewidth of the broad diode laser to reduce decoherence. However, the high-finesse cavity's fringe is not guaranteed to lie at the same frequency as the ion transition. In order to ensure that the light probing the transition is in resonance with the transition, one can shift the frequency of the laser light either going into the cavity or going into the trap.

By probing the ion transition with the unlocked laser and comparing it with the location of sidebands on the PDH signal from the high-finesse cavity, we estimated that the cavity frequency was approximately 130 MHz higher than the frequency of the ion transition.

Two locations of frequency shifts exist in our setup: those from the fiber-noise cancellation and those from the control board. We use one AOM at 330 MHz for the fiber-noise cancellation going to the cavity and one AOM centered at 200 MHz diffracted into the -1 mode for the fiber-noise cancellation going to the control board. All three of the AOMs on the control board can be set to shift the frequency of the light after double-pass between 300 and 500 MHz.

A diagram of the frequency shifts of the beams is in Figure 12. The light from the probe beam is shifted by 330 MHz from the fiber-noise cancellation. This causes the laser to be locked 330 MHz below the cavity frequency. The light from the main beam is shifted by -200 MHz at the fiber-noise cancellation and then later by 400 MHz at the control board. These three shifts add such that the frequency of the light at the trap is 130 MHz lower than the cavity frequency.

[5]OZ Optics LTD PMJ-3A3A-633-4/125-3-(length)-1

4.2 Fiber-Noise Cancellation

Fiber-noise cancellation will be performed for both the main and probe beams. The setup includes one AOM for noise cancellation of the main beam and one for the probe beam. A diagram of the fiber-noise cancellation section of the setup can be found in Figure 13.

Both AOMs used for the fiber-noise cancellation are made by AA Opto Electronics. The active apertures are quite small. The 200 MHz AOM[6] has an active aperture of 0.5 mm, and the 350 MHz AOM[7] has an active aperture of 0.12 mm. The recommended beam sizes are even smaller. Both beams are larger than the active apertures when they leave the laser, so it is necessary to focus the beam down into the AOM.

The main beam needs to be shifted by -200 MHz. The beam size out of the main laser port is about 2.150 mm. The beam passes through a lens of f = 200mm and is focused into the 200 MHz AOM, which is set up in the noise cancellation configuration, though to get a -200 MHz shift, the diffraction orders of the beams are negative from the setup described before. An f = 125mm lens is used to recollimate the beam to the right size for the fiber.

The -1 order is coupled into a fiber which leads to the main control board. After the second pass through the AOM, the +1 and -1 beams are sent back through the f=200mm lens before being picked off by a mirror and sent into a photodiode[8]. The resulting beatnote between the +200 MHz and -200 MHz beams is picked up by the photodiode.

The main beam has a power of 450 mW directly out of the laser port. At the focal point, the power density of the beam is approximately an order of magnitude higher than that for which the AOM is rated. So far, we have not seen any degradation of either the transmission or diffraction efficiencies. To reduce the power travelling through the AOM, we used a pickoff instead of a mirror to retro-reflect the zeroth order into the AOM.

The probe beam needs to be shifted by +330 MHz. The beam out of the probe port is quite elliptical, with dimensions of 2375μm $\times$ 1700μm. The beam size needs to be approximately 1.300mm for optimal fiber coupling. The lenses appropriate for coupling into the fiber were chosen by trial and error since the beam is not perfectly Gaussian.

An f = 200mm lens was used to focus the beam into the AOM. The beam is recollimated after the AOM by an f = 100mm lens. The rest of the setup is identical to the scheme described earlier. The +1 beam is coupled into a fiber which leads to the high-finesse cavity setup. The beatnote for the cavity fiber-noise cancellation setup has not yet been obtained.

4.3 Control Board

The control board splits the main beam into three separate beams. Two of these beams are used for ion control, and the third is used to counter the Stark shift induced by the control beams. A diagram of the setup can be found in Figure 14.

The control beams need to be able to be red or blue detuned from the main transition, and the Stark beam needs to be far detuned from the transition. We use three AOMs centered at 200 MHz in double-pass configuration to achieve these shifts. All three AOMs are diffracted into the +1 order. Because they are double-passed, the total shift of each AOM is centered around 400 MHz. The AOMs[9] used on the control board are manufactured

[6] MT200-B100A0
[7] MT350-B120A0
[8] KPD 130
[9] ATM-2001A2

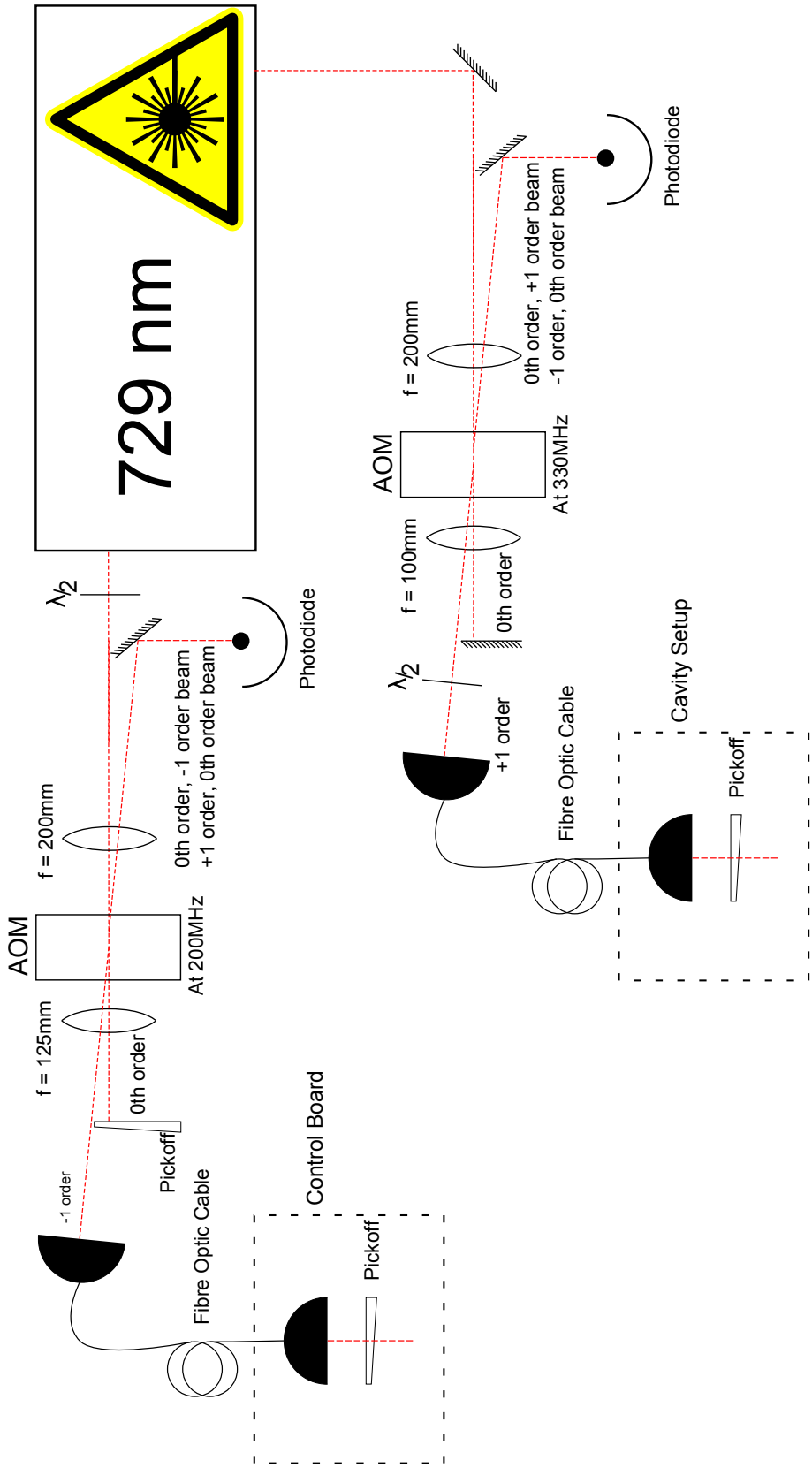

Figure 13: Optical layout of the fiber-noise cancellation setup. There are two beams that need fiber-noise cancellation: the beam going to the ion and the beam going to the cavity.

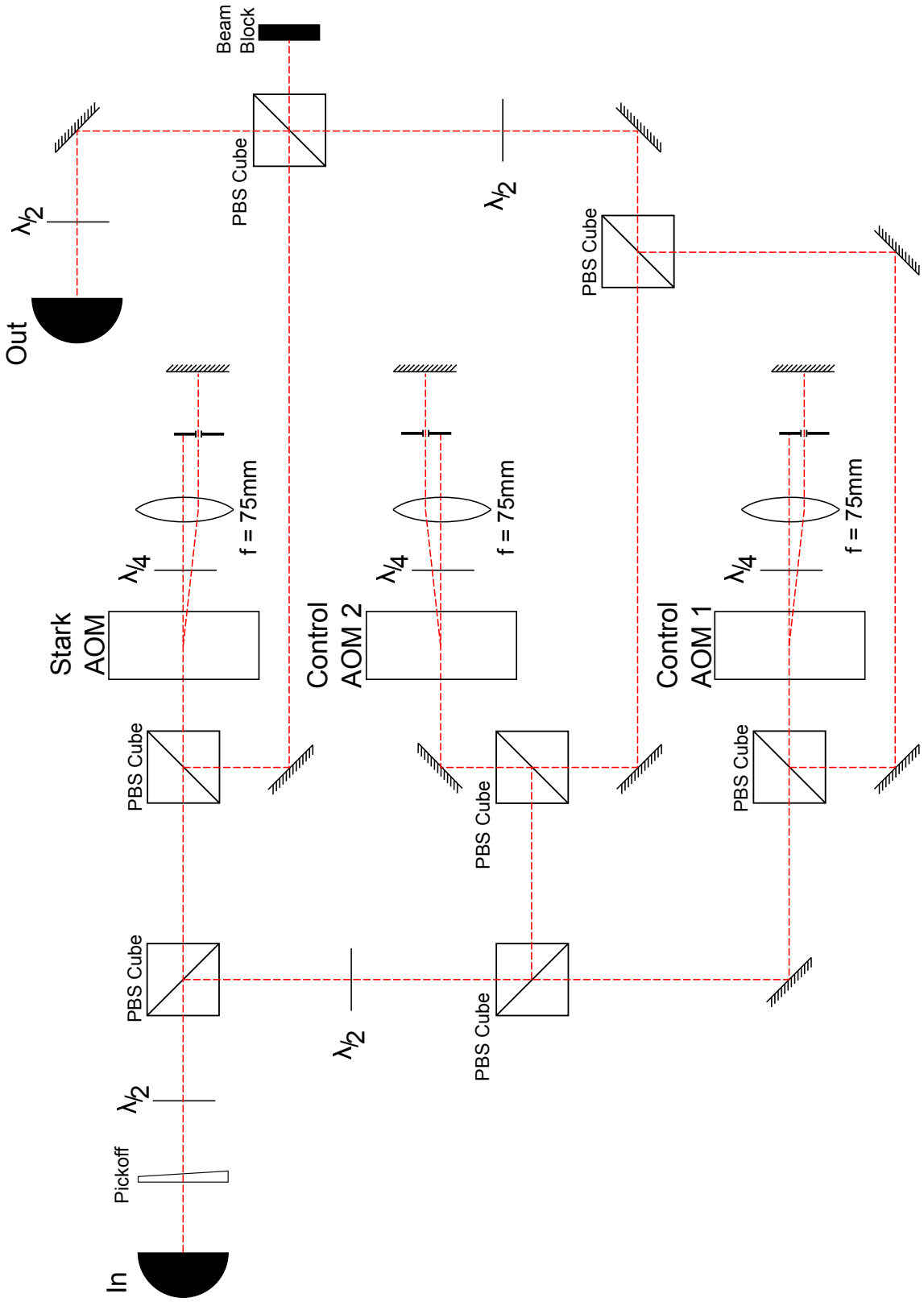

Figure 14: Optical diagram of the control board.

by IntraAction and have an active aperture of 1mm. The beam in the setup is already 1.150mm, so it is not necessary to focus the beam down further into the AOMs.

The beam enters the setup via a 10m fiber terminating in a fixed-focus fiber collimator. Immediately the beam hits a pickoff, which reflects about 4% of the light back into the fiber for the fiber-noise cancellation. The rest of the light continues into the setup. With half-wave plates and polarizing beam splitters, the beam is split into three beams. These three beams are double-passed through the AOMs. The two control beams are recombined using a polarizing beam splitter. Their polarizations are subsequently rotated 45 degrees using a half-wave plate. This beam is then combined with the Stark beam. The control beams lose 50% of their power in this configuration, and the extra light is blocked with a beam block. The resulting combination of the three beams is then directed into a fiber collimator.

4.4 Beam Delivery

The beam is transported from the control board to the beam delivery board via a 2m fiber. The breadboard for the beam delivery sits above the main table at a height of 25 cm. This gives a beam height of 30 cm, at the height of the trap. The breadboard screws into the mount for the coils and is further supported by 4 legs that are clamped to the table.

The beam passes through a coupler to a pickoff and then continues to a precision mirror mount. This mount has micrometer screws for adjusting the position of the beam onto the ion.

To focus onto the ion, the beam travels through the focusing box, which is mounted on the trap setup. In the focusing box, the beam first passes through a 200mm lens and hits a dichroic beamsplitter. The dichroic beamsplitter passes most of the 729 nm light while reflecting a small portion onto a mirror, which reflects the light back onto the beam delivery board. Once back on the beam delivery board, the beam passes through a pickoff. The picked off light is reflected into a camera[10] for positioning the beam, and the light that continues through the pickoff is directed into a photodiode[11] for optical power monitoring. A diagram of the optical setup is in Figure 15.

4.5 High-Finesse Cavity

The 729 nm laser has a specified linewidth of 100 kHz integrated over 5 μs. Ideally this linewidth should be narrowed down to the Hz regime in order to maximize coherence time. The details of how PDH locking is employed to narrow the linewidth can be found in Martin Sepiol's thesis [19]. In Sepiol's thesis, the cavity table also includes an AOM setup to shift the frequency of the laser to hit the ion resonance. This portion was removed since we now employ those shifts in other areas of the setup. A diagram of the current HFC setup can be found in Figure 16.

The beam is delivered to the table via a fixed-focus fiber collimator. The beam first hits a pickoff, which sends around 4% of the light back through the fiber for the fiber-noise cancellation.

The beam size out of the fiber is approximately 1300μm. The fiber that goes into the EOM, however, needs a beam size of 2000μm. This is a magnification factor of around 1.5. A telescope was therefore placed between the two fibers using lenses of focal lengths 50mm and 75mm. After passing through the telescope, the beam is coupled into the fiber leading

[10] Point Grey Firefly MV
[11] ThorLabs PDA36A-EC

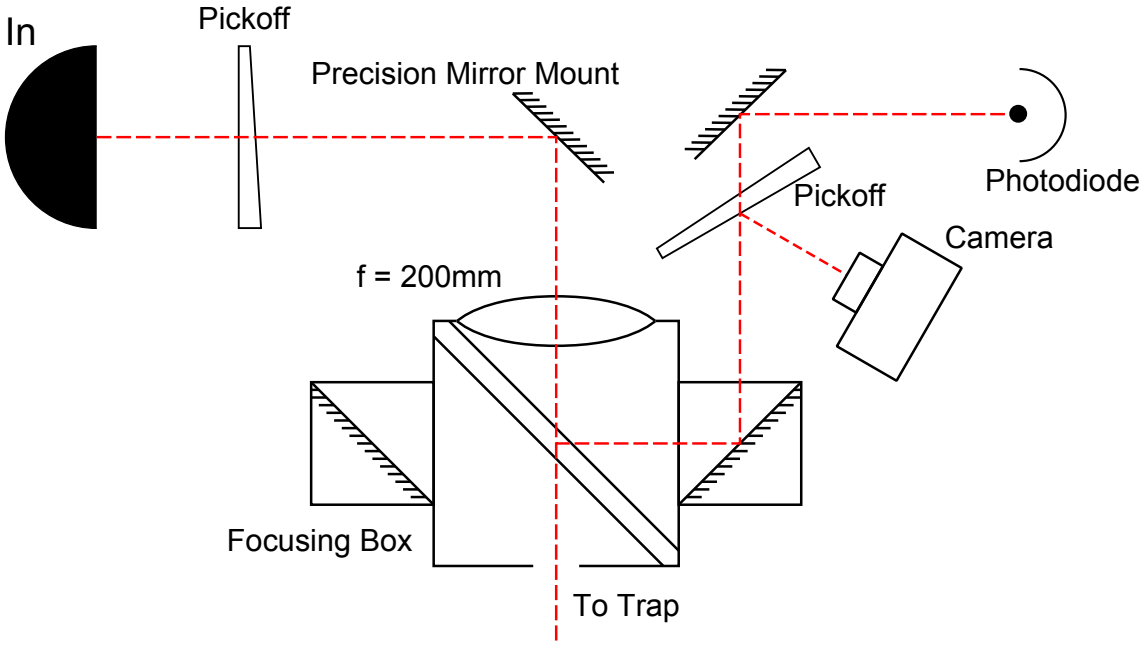

Figure 15: Optical layout of the 729 nm laser beam delivery to the trap.

to the EOM. Using the telescope, fiber coupling efficiency, including the pass through the EOM, was improved from 11% to 19.5%.

The rest of the setup is unchanged from Sepiol's thesis and is used for PDH locking of the laser to the cavity.

5 Setup Characterization

5.1 AOM Input Power

The AOMs are powered by a frequency source which is in turn fed into an amplifier. The amplified RF power is then fed to the AOMs. For the following tests, the frequency source used for control AOM 1 was an AtlanTecRF source[12], capable of a range of 160 to 220 MHz. The amplifier used for control AOM 1 was a MiniCircuits instrument amplifier[13], which has a gain of approximately 45 dB at 200 MHz. The frequency source used for control AOM 2 and the Stark AOM was a TTi source[14]. The amplifier used for these two AOMs was a homebuilt amplifier[15] followed by a MiniCircuits amplifier[16], which together have a gain of approximately 38 dB at 200 MHz.

The optimal operating power for these AOMs was found by aligning the AOM and then stepping up the power until the diffraction efficiency was maximal. A directional coupler[17] was placed after the RF amplifier to measure the RF power into the amplifier.

The optimal operating power for control AOMs 1 and 2 at 200 MHz was found to be about 31 dBm. The optimal operating power for the Stark AOM at 200 MHz was found to be about 29 dBm.

[12] AtlanTecRF ANS3-0160-001
[13] TIA-1000-1R8-2
[14] TGR2050
[15] Amp06
[16] ZFL-1000VH2
[17] ZFBDC20-62HP-S+

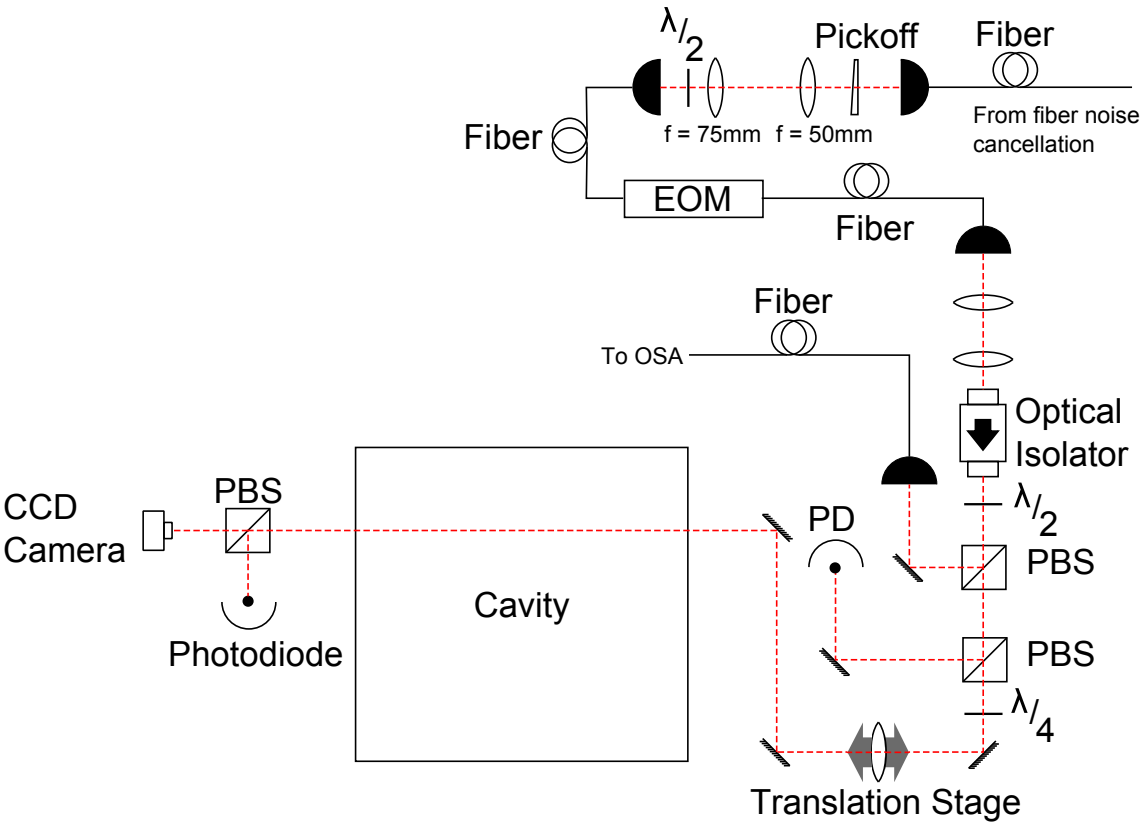

Figure 16: Optical layout of the high-finesse cavity table.

The fiber-noise cancellation AOMs were driven by a Rohde and Schwarz frequency source[18]. For the fiber-noise cancellation AOMs, the maximal operating power is specified for the two AOMs, so the power was not stepped beyond that limit. The 350 MHz AOM cannot be operated above 31.1 dBm, and the 200 MHz AOM cannot be operated above 33.4 dBm. The 350 MHz AOM is run at maximum power. The 200 MHz AOM is run at approximately 32.3 dBm.

5.2 AOM Efficiency

The dependence of diffraction efficiency on frequency was measured for the 200 MHz Intra-action AOMs on the control board for both single-pass and double-pass configurations. The efficiencies were aquired with a power meter by first measuring the total incoming power and then measuring the first order power. The first order power was divided by the incoming power.

Plots of the efficiencies of the single-pass can be found in Figure 17. The plots show the maximum diffraction efficiency along with the RF power that achieved that efficiency for control AOMs 1 and 2. To measure this, the RF power from the RF source was stepped at each frequency until a maximal optical power was seen. The corresponding actual RF power was measured using a directional coupler placed before the AOM which fed into the RF spectrum analyzer. The AOMs were not realigned at each frequency.

The power maximizing the diffraction efficiency is also plotted in Figure 17. The data shows that the RF power necessary for maximizing the diffraction efficiency follows

[18] SMC100A

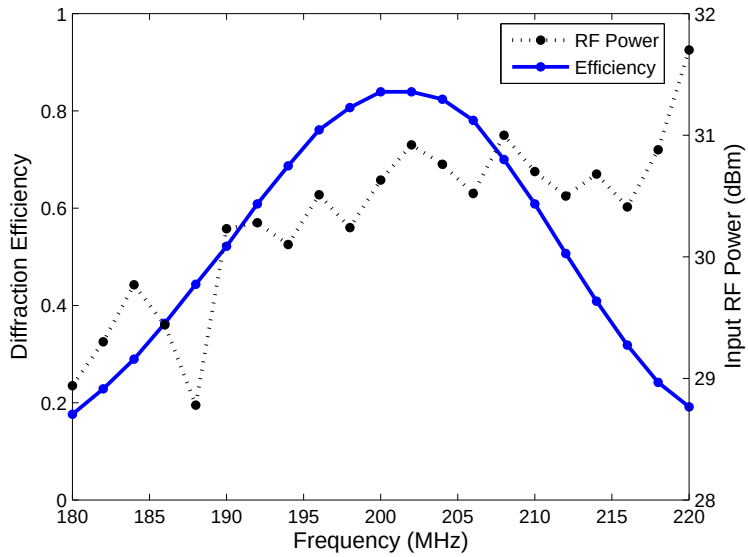

(a) Control AOM 1

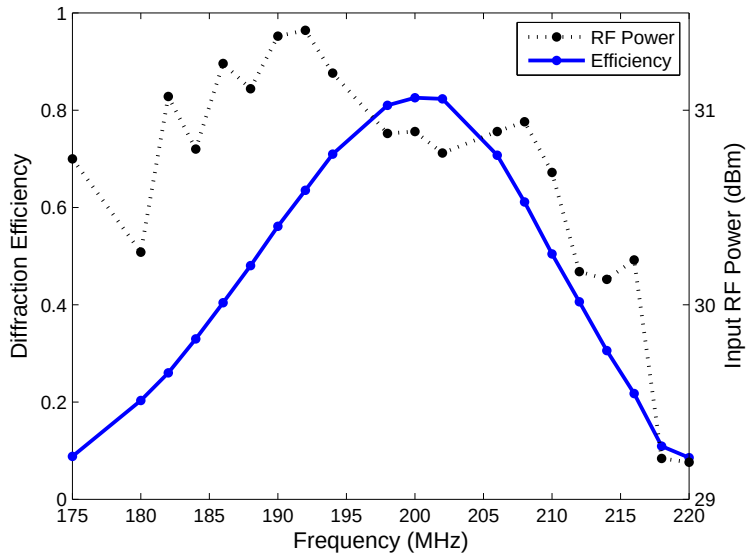

(b) Control AOM 2

Figure 17: Maximal diffraction efficiency along with the power that optimized the efficiency over a range of frequencies. (a) shows this for control AOM 1, whereas (b) shows it for control AOM 2.

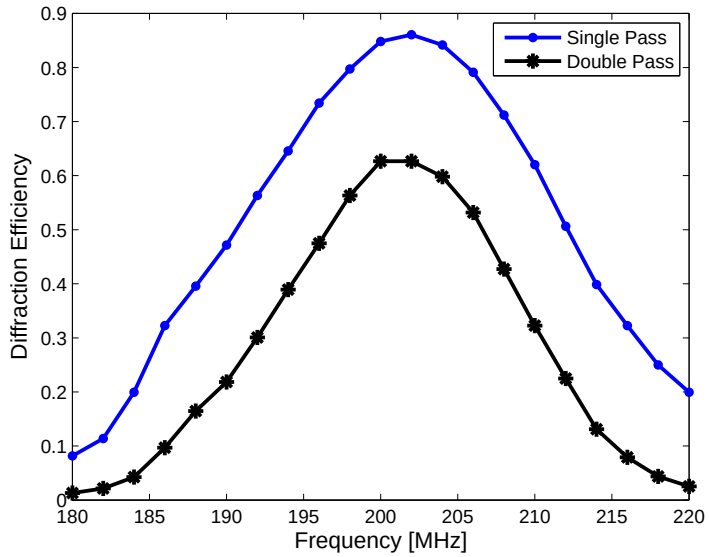

Figure 18: The single-pass and the double-pass efficiencies are compared for control AOM 2. The double-pass efficiency is approximately the square of the single-pass efficiency. The frequency plotted is the RF frequency at which the AOM is driven rather than the frequency of the light shift, which would be double for the double-pass.

opposite trends for the two AOMs. It is therefore necessary to independently calibrate each AOM if maximal optical output power is desired.

A plot showing the single-pass efficiency plotted with the double-pass efficiency for control AOM 2 can be found in Figure 18. This measurement was taken by stepping through frequencies on the RF source. The frequency plotted for the double-pass curve is the frequency which was input to the AOM. The shift frequency of the light is double this value.

In the experiments, the AOMs are controlled by DDS (direct digital synthesizer) which is fed into an RF amplifier. The DDS is controlled by the computer, so the RF power going to the amplifier is easily set for a given frequency. The DDS is calibrated such that, over the range of an experiment, the optical power coming out of the AOM is maintained no matter to which frequency it is tuned. The calibration is further explained in Section 6.

5.3 AOM Pickup

One concern was that the three AOMs on the control board would be close enough together that they would pick up the frequencies of the others. If one AOM picks up the frequency of another AOM, diffraction will occur at the picked-up frequency as well as at the main frequency. [20] The small amount of light from the picked-up frequency will introduce errors in a quantum gate. An RF spectrum analyzer was used to probe the pickup by monitoring the RF spectrum of an AOM while detuning the frequency of one of the other AOMs.

Control AOM 1 was run at 200 MHz while the frequency of either control AOM 2 or the Stark AOM was varied. A small peak appeared in the RF spectrum of control AOM 1 at the frequency of the second AOM. A graph of the interference between the AOMs is provided in Figure 19. The y-axis shows the magnitude of the small peak in dBm. The

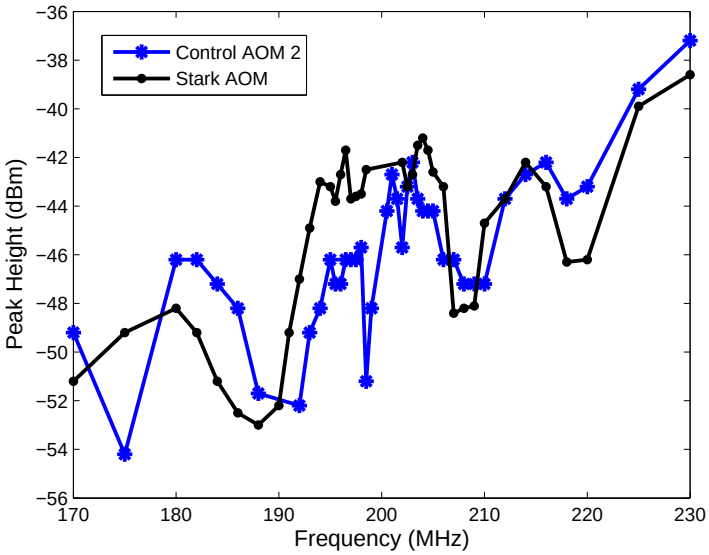

Figure 19: Measurement of the effect of one AOM on another. Control AOM 1 is run at 200 MHz while the frequencies of control AOM 2 and the Stark AOM are varied (in independent trials). One sees a peak in the spectrum of control AOM 1 at the frequency of the second AOM, the height of which is measured and presented as the y-axis in this plot.

main frequency (200 MHz) had a height of approximately 34 dBm.

The Stark AOM and control AOM 2 have a similar effect on control AOM 1. Thus, which AOM is chosen for each beam does not seem to be important. One noticeable thing was that there was no pickup of signal until the amp for control AOM 1 was turned on, whether or not the frequency source was on. This observation suggested that the amp might be amplifying a small signal.

However, by moving the amps away from one another to see if they were picking up a signal from one another, the cables leading to the AOMs were also moved. Without moving the amps and just moving the cables, the unwanted peak was reduced to the level of the noise floor of the spectrum, which may indicate crosstalk between the cables. It seems to be that more important than separating the amps and the AOMs is keeping the cables from picking signals up from one another.

5.4 Losses

A table of the losses and efficiencies documented in this section can be found in Appendix B.

5.4.1 Main Beam

For the fiber-noise cancellation for the control board, the 200 MHz AOM has 84% diffraction efficiency at 200 MHz. This is the only major loss in the fiber-noise cancellation section for the main beam.

The fiber coupling efficiency from the fiber-noise cancellation setup to the control board is about 52% (including the pickoff). After the first beamsplitter (BS1), a maximum of 96% and a minimum of 1.1% of the light continues toward the Stark shift AOM. A maximum of

90% and a minimum of 0.7% of the light is reflected down the other branch. This branch splits into two after the second beamsplitter (BS2). When a maximum amount of light is travelling down this branch, a maximum of 87% of the light travels toward control AOM 2, and a maximum of 86% of the light travels toward control AOM 1.

Before each AOM is another beamsplitter for the separation of the incoming and the double-pass beam. For the Stark AOM, there is a surprising amount of loss at this beamsplitter (BS-AO3) in the forward direction. Only around 80% of the light passes through the beamsplitter. For control AOM 1, around 97% of the light passes from the beamsplitter (BS-AO1) into the AOM, and for control AOM 2, around 98% of the light passes from the beamsplitter (BS-AO2) to the AOM. The cause of the large loss in the Stark AOM beamsplitter is unclear.

Control AOM 1 has a double-pass diffraction efficiency of 66%, control AOM 2 has a double-pass diffraction efficiency of 68.6%, and the Stark AOM has a double-pass efficiency of 57.2%. The double-pass efficiencies include the second pass through the beamsplitter, so any losses acquired due to the beamsplitter are included in these percentages. For control AOMs 1 and 2, this efficiency includes the beamsplitter that is used to recombine the beams. For the Stark AOM, the efficiency includes the beamsplitter used to combine the three beams. The losses from these two beamsplitters were minimal. At the second recombining beamsplitter, the two control beams each lose approximately 50% of their power.

By multiplying all of these percentages, we calculate that at maximum power for each beam (other two minimized), the Stark beam can have 23% of the light from the fiber-noise cancellation going into the fiber towards the beam delivery, control AOM 1 can have 13%, and control AOM 2 can have 14%.

The fiber coupling efficiency for the three beams to the beam delivery board differs slightly. Control beam 1 has an efficiency of 63.7%, control beam 2 has an efficiency of 56.4%, and the Stark beam has an efficiency of 58.4%. There are no further large losses in the beam delivery.

Combining the three setups, the total efficiency for control beam 1 is 7%, for control beam 2 is 6%, and for the Stark beam is 11%. Therefore, for a beam out of the 729 nm laser of 450 mW, a maximum of 31.4 mW, 28.8 mW, and 50.4 mW can reach the ion for control beam 1, control beam 2, and the Stark beam, respectively.

5.4.2 Probe Beam

The 350 MHz AOM used for fiber-noise cancellation of the probe beam has a diffraction efficiency of 60%. The fiber coupling between the fiber-noise cancellation and the high-finesse cavity setup has a coupling efficiency of approximately 60%. 4% of the light is reflected back by the pickoff, so 96% of the light continues to the fiber coupler. The fiber coupling through the EOM has an efficiency of 19.5%. Therefore, about 6.7% of the light into the AOM can be used for the laser locking. Because the HFC does not require much light for locking, this is sufficient.

There is a difference in intensities between the two beams creating the beatnote for the fiber noise cancellation. In both the main and probe beam setups, the signal due to the light that travels down the fiber is less intense at the photodiode than the beam that does not travel down the fiber. For the 200 MHz AOM, the difference in intensities is only due to the 56% decrease in power from the fiber coupling on the fiber signal. For the 350 MHz AOM, there is a difference between the two due to both the 60% fiber coupling efficiency as well as the 4% loss from the pickoff. In short, the ratios of the powers of post-fiber

signal to the pre-fiber signal are .56 for the 200 MHz AOM, and .024 for the 350 MHz AOM.

5.5 Beatnote

5.5.1 Obtaining a Beatnote

We ran into many challenges when trying to measure the beatnote for the fiber-noise cancellation. The aim of this section is to ensure that others do not experience the same troubles as we did.

At the end of the 10m fiber, the outgoing beam emerges from the fiber coupler and is partially reflected by the pickoff. The reflected beam has only 4% of the power of the outgoing beam. One cannot block the outgoing beam without also losing the reflected beam. Therefore, seeing if the two beams are overlapped is very difficult. The pickoff is located close to the fiber coupler and therefore makes overlapping the beams even more difficult for two reasons. First, seeing between the coupler and the pickoff is difficult, and so it is hard to see the two beams that need to be overlapped. Second, it is only possible to see the reflected beam when it is not overlapped with the outgoing beam. The pickoff is mounted in a mirror mount. The ability to move the beam off of and back onto the outgoing beam in a smaller number of mirror mount screw turns would have been helpful, in order to get an idea for the x- or y-displacement from the center of the beam. In the future, one should consider ease of visual beam overlap versus ease of maximizing the signal once the beams are partially overlapped when deciding how far apart to place the pickoff from the fiber coupler.

Another challenge was that we tried to couple the reflected beam into the fiber by maximizing the beatnote while looking at the signal from the photodiode on the RF spectrum analyzer. Difficulty arose because a peak at 400 MHz was present without the reflected light coupled down the fiber. This peak may be due to the presence of first order light in the zero order beam. As a result, it was impossible to see changes in the spectrum when only some of the reflected light was coupled into the fiber, and therefore hard to optimize.

To finally couple light down the fiber, a quarter-wave plate was placed between the fiber coupler and the pickoff. A polarizing beamsplitter was placed in the beam path after the AOM but before the fiber. Because the reflected light passes through the waveplate twice, the beam is rotated by 90 degrees and is reflected by the beamsplitter. A photodiode[19] was used to measure the power of this beam, maximizing the coupling was possible.

One last aspect of obtaining the beatnote is overlapping the reflected beam from the fiber with the reflected beam from the mirror after the second pass of the AOM. The location of the beam from the fiber is fixed, but the beam reflected by the mirror depends on the angle of the mirror. Ideally, the mirror would be perpendicular to the beam it reflects. In practice, this alignment is challenging. Two methods exist to overlap these beams. If there is enough power in the beam from the fiber, the beam from the mirror can be visually overlapped with the beam from the fiber, and then be improved by maximizing the signal in the beatnote. If there is not enough power to see the beam from the fiber (for example, possibly for the cavity fiber-noise cancellation setup), one can disconnect the long fiber from the fiber coupling and instead send a separate beam through the AOM. This method allows one to overlap the beam from the mirror with a visible beam from the fiber.

[19] ThorLabs PDA36A-EC

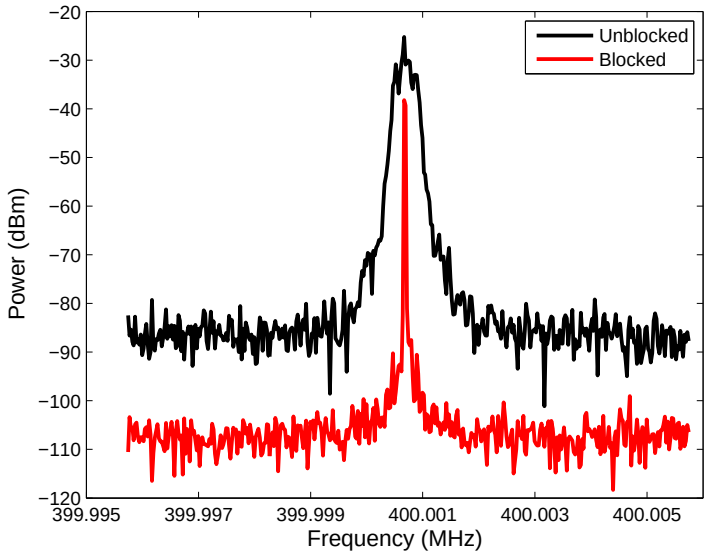

Figure 20: Beatnote measurement for fiber-noise cancellation of the main beam. The black (top) curve shows the signal from the photodiode when both the beam reflected after the fiber and the beam reflected before the fiber interfere. The red curve shows the signal when the beam going to the fiber is blocked before the beam reaches the fiber coupler.

5.5.2 Measurement

Once the reflected beam had been coupled into the fiber, we were able to see a change in the signal of the beatnote. A comparison of the peak with and without the light from the fiber is shown in Figure 20. The black peak shows the beat signal of the positively and negatively shifted light that is coupled into the photodiode. The red peak is the signal from the photodiode when the beam entering the fiber is blocked.

There are three distinct differences between the peaks. Firstly, the black peak is taller than the red peak, as we expect. Secondly, the black peak is wider. This is the broadening we expect to see due to the fiber-noise. Thirdly, the 'noise floor' is higher. This seems strange until we consider the range of frequencies shown in the plot, only spans about 10 KHz. The beat is shown in Figure 21 with a wider range. As is visible in this plot, the noise spans a wider range than is shown in the first plot.

When whistling, we were able to see a new peak form in the spectrum. The peak from the whistling is only visible when both both beams are present. The peak is therefore due to noise induced on the long fiber, and not in another part of the setup.

6 Measurement Techniques

The state of the calcium ion is probed using the 397 nm transition. If the ion is in the $|\downarrow\rangle$ state, the ion fluoresces. If the ion is in the $|\uparrow\rangle$ state, the ion is dark. The fluorescence can be seen by using a CCD camera where the ion is visible when it is in the $|\downarrow\rangle$ state and disappears when it is in the $|\uparrow\rangle$ state. The fluorescence is measured using a photomultiplier tube. One can switch between the camera and the photomultiplier tube using a flip mirror.

The experiments are computer controlled. Because the control and Stark AOMs are controlled by the computer, their frequencies and powers can be scanned in an experi-

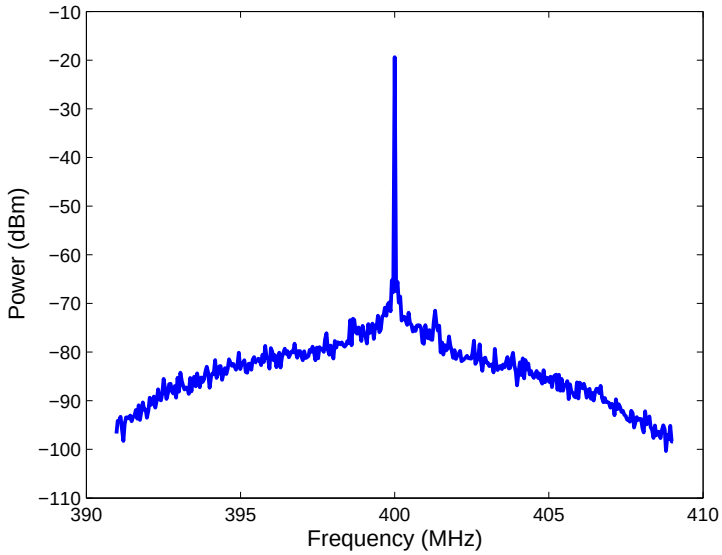

Figure 21: Beatnote for main beam fiber-noise cancellation.

ment. It is also possible to program pulse sequences of the various lasers to set up a full experiment. Data acquisition from the photomultiplier tube is also done by the computer.

As mentioned before, the DDS can be programmed such that over all frequencies, the optical power delivered to the ion will be approximately constant. The DDS output amplitude is controlled by a factor between 0 and 1, where 0 is no power and 1 is full power. The following explains how the program estimates what this factor needs to be in order to maintain constant optical power.

A table of a few frequency points and their corresponding powers is used in order to estimate the optical power going to the ion. This table is plotted in Figure 22. The power here is measured as a voltage from the photodiode on the beam delivery board. The optical power at the frequency that has the lowest maximum optical power is chosen to be the value of the optical power delivered for all frequencies.

We estimate the optical power between two points to have a roughly linear relationship. The program finds the two frequencies in the table closest to the actual frequency and linearly interpolates to find the approximate maximum optical power at the actual frequency. The estimated power is compared to the desired constant power in order to get the factor for the DDS amplitude.

7 Preliminary Measurements

7.1 Ca^+ Spectrum: Low Field

At first, we did not know what the offset between our cavity frequency and our ion transition frequency was. We first measured the cavity frequency with the wavemeter to get an estimate of the difference, assuming that it was within about 50 MHz of the actual frequency. We estimated that the frequency of the cavity was approximately 40 MHz higher than the transition frequency.

To find the correct relative shift between the cavity and ion frequencies, we needed to scan an AOM frequency to see what frequency causes transitions between the $S_{1/2}$ and $D_{5/2}$ states. We first tried to probe the transition of the ion at low field, since it is easier

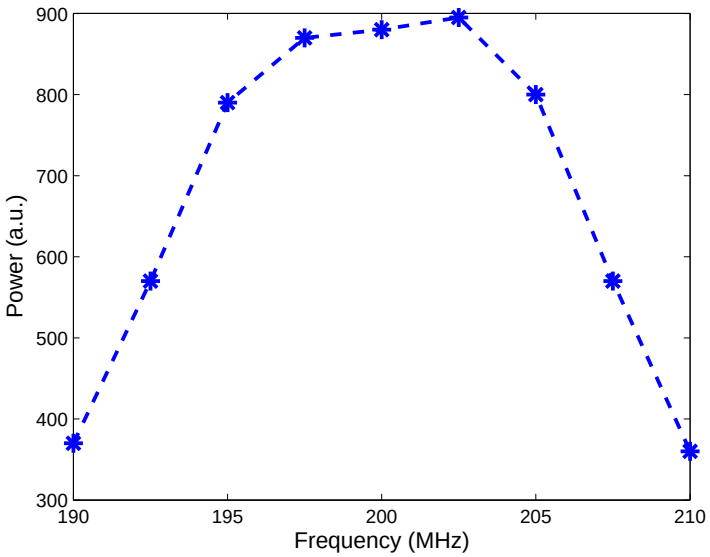

Figure 22: DDS calibration table, plotted.

to probe than the transition of the ion at high field. This is because at low field, the splitting between the m states is very small, and therefore more states are available for the transition. It is also not important to prepare the S state in a specific state, so it did not require setting up pulse sequences to probe.

The transition frequency of the ion at low field is about 133 MHz lower than the transition at high field. Using our estimation of the cavity frequency, the difference between the ion transition frequency at low field and the cavity frequency would be 170 MHz.

We wanted to probe this transition before putting in all of the noise cancelling AOMs, in case we needed a different frequency shift than expected. Instead of the two AOMs, only the 350 MHz AOM was placed before the cavity. This AOM was operated at the edge of its range at 290 MHz. The only other AOM involved was the Stark AOM. The Stark AOM can shift the frequency between 300 and 500 MHz.

Lastly, in another attempt to make the transition easy to find, we used a lot of power for the 729 nm beam. Initially we put about 28 mW of light into the trap.

To probe the transition, we first loaded five ions into the trap. Upon turning on the 729 nm beam and minorly adjusting the position, we saw quantum jumps in the ions. These jumps manifested themselves as the $^{40}Ca^{+}$ fluorescence decreasing as an ion shelved into the $3^2D_{5/2}$ state. Fluorescence is detected on the 397 nm transition. Therefore, when the $D_{5/2}$ state is occupied, and therefore the $S_{1/2}$ state is unoccupied, there will be no fluorescence because the ion cannot complete the $S_{1/2} \rightarrow P_{1/2}$ transition.

The 397 nm beam was on during this experiment such that the ion fluorescence could be probed. The 866 nm beam was also turned on to pump the ions out of the $D_{3/2}$ state such that decay into this state did not look like a jump into the $D_{5/2}$ state.

A plot of this effect can be seen in Figure 23. A quantum jump has occurred when the fluorescence decreases. At the time that this data was recorded, we had lost two ions due to heating, so there were only three ions in the trap. It is unclear why there are not three distinct signal amplitudes for one, two, and three ions being dark.

We then tried tuning the frequency of the AOM using the Rohde and Schwarz frequency source to see the region in which quantum jumps were occurring. This was problematic

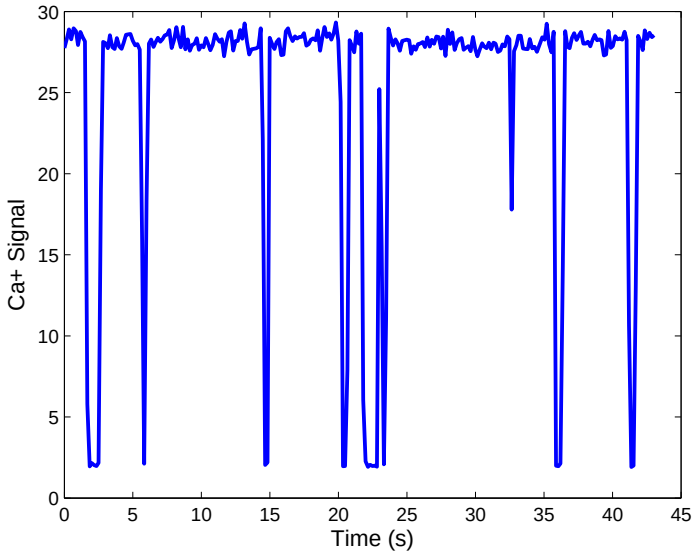

Figure 23: Calcium fluorescence over time. Dips in the fluorescence indicate a shelving event due to the 729 nm beam causing an $S_{1/2} \rightarrow D_{5/2}$ transition.

because as we scanned over the AOM frequencies, the optical power changed (see Figure 18). Thus, rather than probing the frequency dependence, we were probing the power dependence.

We then switched to using the DDS for the control of the AOM frequency such that we could keep the optical power constant over the frequency range. Once we switched to this, we realized that we were only probing the transition due to the high power and not due to being on resonance.

7.2 Ca^+ Spectrum: High Field

After not being able to find the transition at low field, we decided try at high field. At this point, we estimated the cavity frequency by probing the ion with the unlocked laser, as described in Section 4.1, and put in the second fiber-noise cancellation AOM at -200 MHz.

To do spectroscopy on the $4^2S_{1/2}$ $m = 1/2$ to $3^2D_{5/2}$ $m = 3/2$ transition, we probed the ion using the following pulse sequence

1. Doppler Cooling with the 397 nm laser and 866 nm laser
2. State Preparation with the 397 nm laser ($\sigma+$) and 866 nm laser
3. Shelving with the 729 nm laser
4. Detection with the 397 nm laser and the 866 nm laser
5. Repumping with the 854 nm laser

Shelving counts were determined by a cut off where fewer than 4 photons were detected.

By scanning the frequency of the Stark AOM, we were able to narrow down the location of the transition. By scanning over a small range with a large number of data points, we obtained the spectrum plotted in Figure 24. For this set of data, the pulse times were

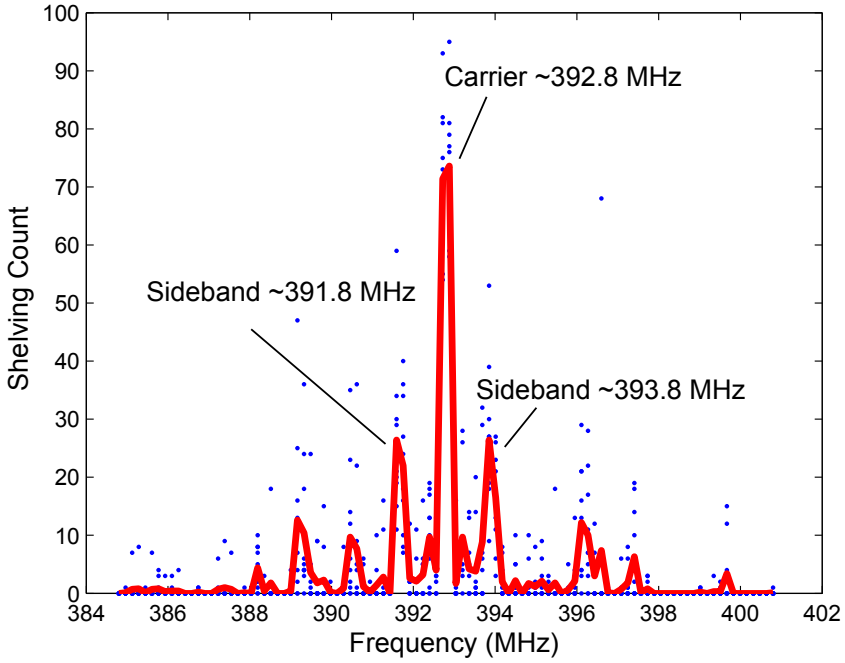

Figure 24: Spectrum of $4^2S_{1/2}$ $m = 1/2$ to $3^2D_{5/2}$ $m = 3/2$ transition. The red curve shows the averaged data, whereas each point represents one scan. The peak in the middle is the carrier transition and the large peaks on the sides are the axial sidebands. The frequency on the x-axis is the total shift acquired on the AOM board.

1. Doppler Cooling: 100 μs
2. State Preparation: 100 μs
3. Shelving: 4 μs
4. Detection: 400 μs
5. Repumping: 400 μs

The frequency to the AOM was scanned over a span of 8 MHz with the center frequency at 196.4 MHz. The plot, however, shows the doubled frequency since the AOM is double-passed. The data acquisition works such that at each frequency it probes, 200 experiments are carried out before switching frequencies. The frequencies are then scanned over 100 times, to give a total of 20000 experiments. The blue data points in the graph show the averaged 200 experiments, and the line in the graph traces the average between the points at the same frequency. Shelving is determined when the detected photons are fewer 5.

The carrier transition is at approximately 392.8 MHz, and the axial sidebands sit approximately 1 MHz away on either side. The smaller peaks to either side of the carrier transition are the lobes of the carrier transition. The ion was not well cooled, so we expect to see higher order sidebands, possibly explaining the presence of other peaks in the spectrum.

The excited state population of the carrier transition is given by the following equation

$$P_n(|\uparrow\rangle) = \frac{\Omega_{R,n}^2}{\Omega_{R,n}^2 + \delta^2} \sin^2(\sqrt{\Omega_{R,n}^2 + \delta^2} t/2) \tag{16}$$

where t is the 729 nm pulse time and n is the vibrational number. This basic equation assumes that there is no decoherence and that the ion is in a single vibrational state. Taking into account decoherence, this equation becomes

$$P_n(|\uparrow\rangle) = \frac{\Omega_{R,n}^2}{2(\Omega_{R,n}^2 + \delta^2)}\Big(1 - e^{-\gamma t}\cos(\sqrt{\Omega_{R,n}^2 + \delta^2}t)\Big) \tag{17}$$

where γ is a decay rate. The ion is also not in a single vibrational state. It is in a thermal distribution, given by

$$P_{th} = \left(\frac{\bar{n}}{(\bar{n}+1)}\right)^n \frac{1}{\bar{n}+1} \tag{18}$$

where $\bar{n}$ is the average vibrational number. The Rabi frequency depends on n, and is given by

$$\Omega_{R,n} = \Omega_{R,n=0}\, L_n(\eta^2) \tag{19}$$

where L_n is the nth Laguerre polynomial. Taking into account a thermal distribution, the carrier population is

$$P(|\uparrow\rangle) = \sum_n P_{th} P_n(|\uparrow\rangle) \tag{20}$$

At the Doppler cooling limit, we can estimate $\bar{n}$ to be

$$\bar{n} \simeq \Gamma/(2\omega_t) \tag{21}$$

where Γ is the linewidth of the transition. In our experiement, this is approximately $\bar{n} = 10$. [5]

Figure 25 shows the overdriven carrier transition of an ion cooled near the Doppler limit. This was fit using Equation 20. There was no shelving detection on this experiment, so the curve corresponds to the photon detection signal of the Ca+ ion. The pulse time was 40 μs. The fitted Rabi (n=0) frequency is 41.6 kHz, the decay constant is 1417.3 1/s, the y-offset is 5.9 counts, and the fitted scaling factor is -5.5.

7.3 Rabi Flopping

To see Rabi flopping, we performed the same pulse sequence as before. For this experiment, the frequency of the shelving pulse was fixed, but the time of the shelving pulse was varied. The timing of the pulses is as follows

1. Doppler Cooling: 100 μs
2. State Preparation: 5 μs
3. Shelving: 0-60 μs
4. Detection: 200 μs
5. Repumping: 400 μs

The results of the Rabi flopping experiment are shown in Figure 26. The data shows the average of 2000 measurements at each pulse time. The frequency of the flopping is approximately 43 kHz.

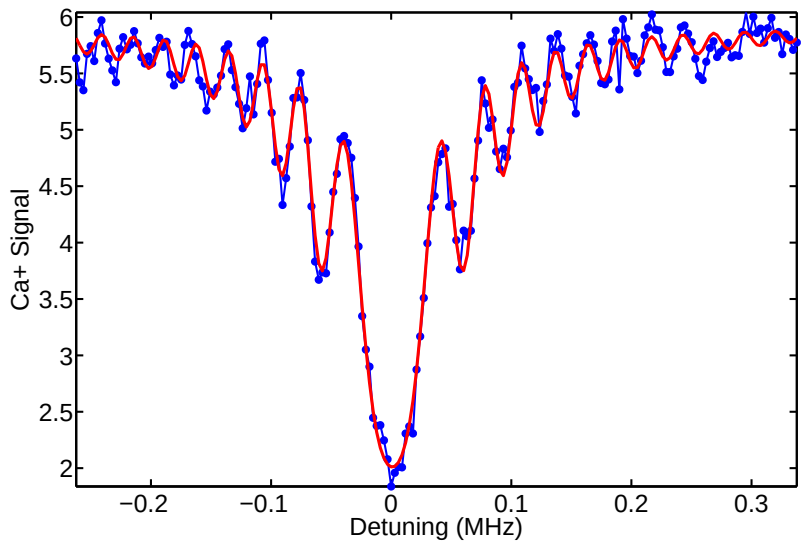

Figure 25: Calcium signal versus detuning for the carrier transition. Actual data is in blue, and the fit to Equation 20 is shown in red.

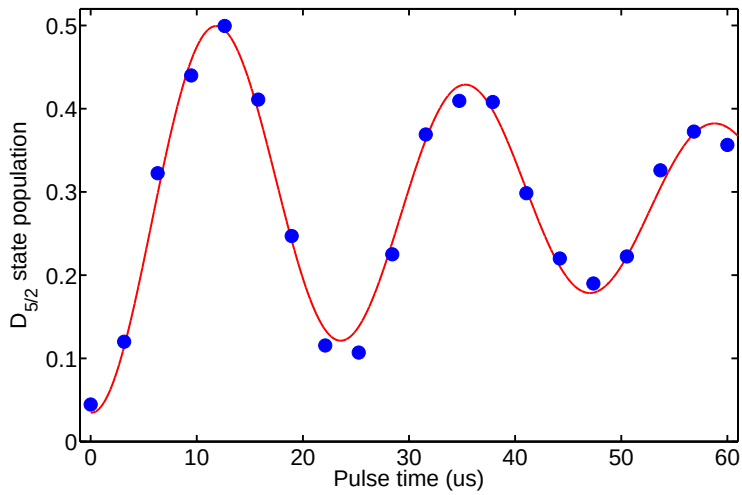

Figure 26: Rabi flops on the $S_{1/2} \rightarrow D_{5/2}$ transition of calcium. Blue points are measured data, and red curve is a fit with frequency 42.6 kHz.

8 Conclusions and Outlook

This thesis describes the construction of a system is used to perform coherent operations on $^{40}Ca^{+}$. It describes the construction of a water cooling and interlock system for the safe operation of field coils as well as the construction of the laser system for coherent manipulations. It also presents some preliminary results from probing $^{40}Ca^{+}$.

The field coils can be operated safely at high current without risk of overheating or flooding. Three 729 nm beams can be focused onto an ion, each of which is frequency tunable over a range of 100 MHz. The frequency of the light that hits the ion is shifted such that the $S_{1/2} \rightarrow D_{5/2}$ $\Delta m = +1$ transition can be probed. The beginnings of a fiber-noise cancellation scheme are in place, with a beatnote having been obtained for the main laser beam.

Quantum jumps were observed, and we obtained a spectrum of calcium around the relevant transition. We were able to identify the carrier and sideband transitions. Finally, we obtained data of Rabi flopping, which showed a Rabi frequency of approximately 43 kHz.

More work remains. At the moment, only the shell of the fiber-noise cancellation is set up. We have obtained only one of the two beatnotes and have not implemented the cancellation itself. It would also be worthwhile to reduce the loss on the AOM board, particularly with the Stark AOM. We are also not yet ready to operate all three beams at once. In order to do this, we need to construct more AOM drivers because currently we have only the supplies to control one at a time. Also, once we start probing the sidebands, we will need to discover exactly how much intensity the Stark beam needs to cancel out the shift in the energy levels.

Despite the list of things that still need to be accomplished, we are close to being able to perform coherent operations on $^{40}Ca^{+}$ with two differently tuned beams and thereby being able to implement more complex quantum gates.

A Appendix I: Interlock Circuit

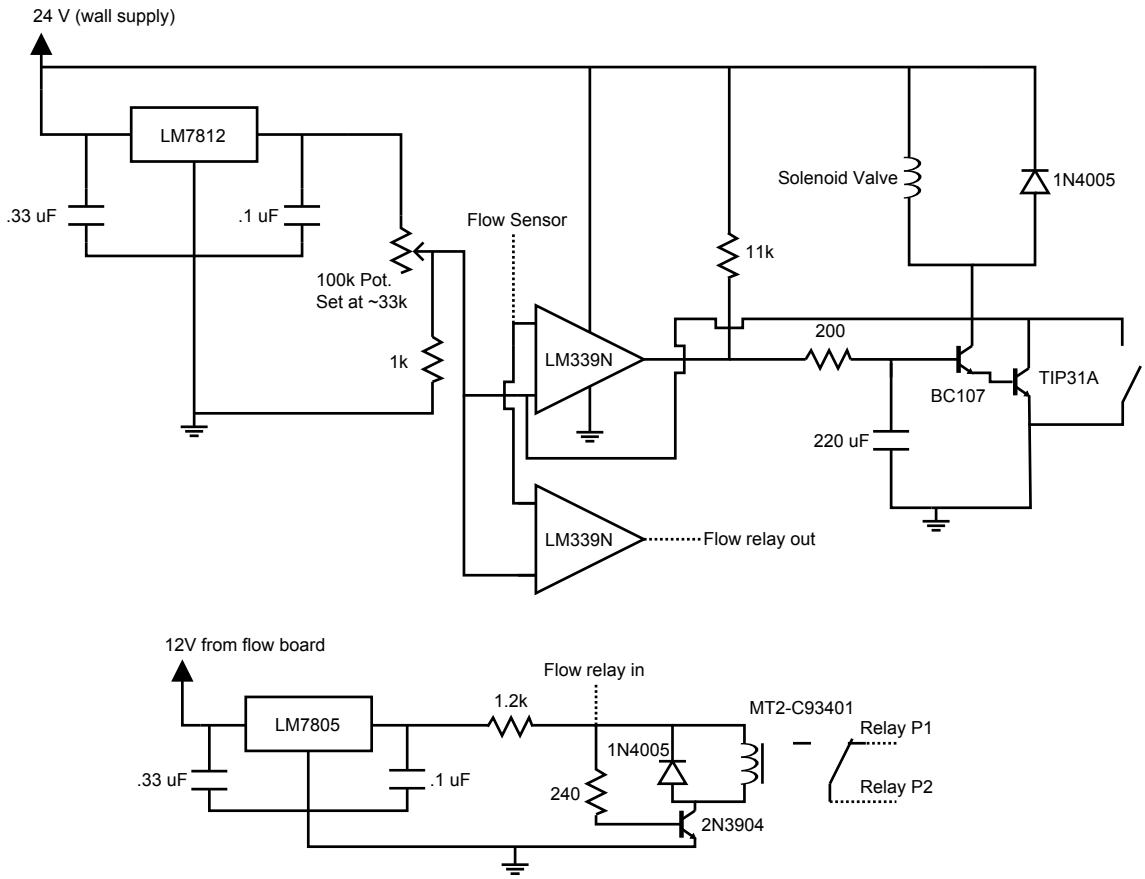

Figure A.1: Flow monitoring board

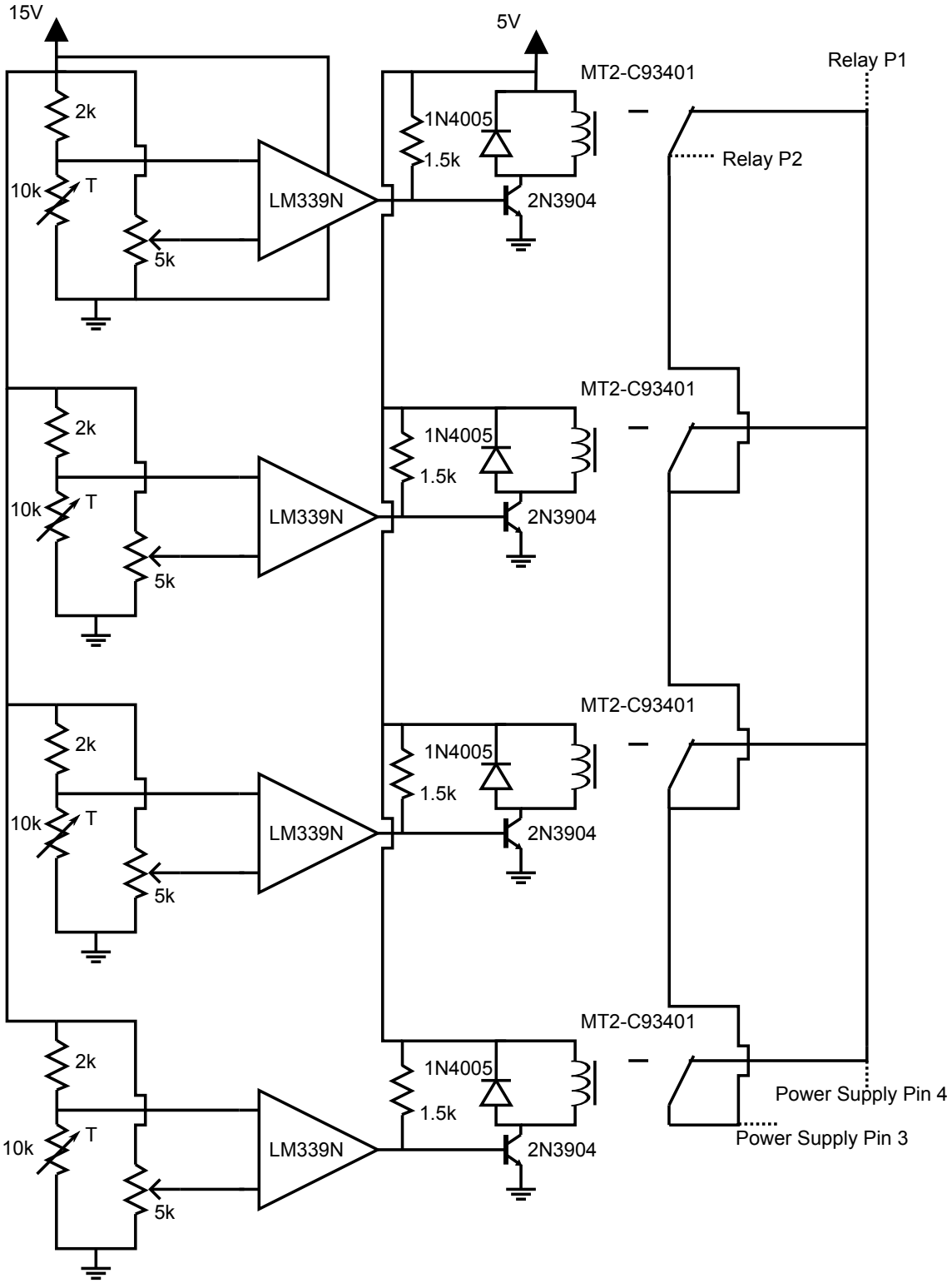

Figure A.2: Temperature monitoring board

B Appendix II: Table of Efficiencies

Fibers	
Fiber	**Coupling Efficiency**
FNC→Control	(incl. pickoff) 0.52
FNC→HFC setup	0.6
Control→Beam Delivery	Depends on beam, see Beam Delivery
HFC setup→EOM→HFC	0.2

Control Board				
AOM	**Single Pass**		**Double Pass (incl. BS)**	
Control AOM1	0.9		0.66	
Control AOM2	0.87		0.69	
Stark AOM	0.84		0.57	
Beamsplitter	**Transmitted**		**Reflected**	
	Max	**Min**	**Max**	**Min**
BS1	0.96	0.01	0.9	0.01
BS2	0.87	0.03	0.86	0
BS-AO1	0.97			
BS-AO2	0.98			
BS-AO3	0.8		0.13	
BS3	negligible losses			
BS4	control beams .50 Stark neg.			
Maximal Efficiencies of Control Board				
Control Beam 1	0.13			
Control Beam 2	0.14			
Stark Beam	0.23			

FNC	
AOMs	**Efficiency**
200 MHz (main)	0.84
350 MHz (probe)	0.6
Ratio of signals at Photodiode	
AOMs	**Ratio of intensities post-fiber:pre-fiber**
200 MHz (main)	0.56
350 MHz (probe)	0.024

Beam Delivery	
Beam	**Fiber Efficiency**
Control Beam1	0.64
Control Beam2	0.56
Stark Beam	0.58

Total maximal light from laser to ion		
Beam	**Efficiency**	**Power (mW)**
Control Beam1	0.07	31.38
Control Beam2	0.06	28.84
Stark Beam	0.11	50.43

HFC Setup	
Pickoff	0.96
EOM and Fiber	(see Fibers)
Total efficiency from laser to HFC	0.07

References

[1] J.I. Cirac and P. Zoller. *Quantum computations with cold trapped ions.* Phys. Rev. Lett., **74**(20), 4091 (1995).

[2] W. Paul. *Electromagnetic traps for charged and neutral particles.* Rev. of Mod. Phys., **62**(3), 531 (1990).

[3] S. Haroche, J.-M. Raimond. *Exploring the Quantum.* Oxford University Press (2006).

[4] C. Roos. *Controlling the quantum state of trapped ions.* Ph.D. thesis, Universität Innsbruck (2000).

[5] J. Eschner, G. Morigi, F. Schmidt-Kaler, and R. Blatt. *Laser cooling of trapped ions.* JOSA B, **20**(5), 1003 (2003).

[6] M. Block, O. Rehm, P. Seibert, and G. Werth. $3d^2D_{5/2}$ *lifetime in laser cooled* Ca^+*: Influence of cooling laser power.* Eur. Phys. J. D **7**(3), 461 (1999).

[7] C. Roos. *Ion trap quantum gates with amplitude-modulated laser beams.* arXiv:0710.1204v4 [quant-ph] (2008).

[8] A. Sørensen and K. Mølmer. *Entanglement and quantum computation with ions in thermal motion.* Phys. Rev. A 62, 022311 (2000).

[9] M. Chwalla. *Precision spectroscopy with* $^{40}Ca^+$ *ions in a Paul trap.* Ph.D. thesis, Universität Innsbruck (2009).

[10] R. Grimm, M. Weidemüller, Y. Ovchinnikov. *Optical dipole traps for neutral atoms.* arXiv:physics/9902072 [physics.atom-ph] (2000).

[11] H. Häffner, S. Gulde, M. Riebe, G. Lancaster, C. Becher, J. Eschner, F. Schmidt-Kaler, and R. Blatt. *Precision Measurement and Compensation of Optical Stark Shifts for an Ion-Trap Quantum Processor.* Phys. Rev. Lett., **90**(14), 3602 (2003).

[12] S. Gulde. *Experimental Realization of Quantum Gates and the Deutsch-Jozsa Algorithm with Trapped* $^{40}Ca^+$ *Ions.* Ph.D. thesis, Universität Innsbruck (2003).

[13] M. Riebe. *Preparation of Entangled States and Quantum Teleportation with Atomic Qubits.* Ph.D. thesis, Universität Innsbruck (2005).

[14] Agilent 6682A Manual. (2009).

[15] E. A. Donley, T. P. Heavner, F. Levi, M. O. Tataw, and S. R. Jefferts. *Double-pass acousto-optic modulator system.* Rev. Sci. Instrum. 76, 063112 (2005).

[16] L.-S. Ma, P. Jungner, J. Ye, and J. L. Hall. *Delivering the same optical frequency at two places: accurate cancellation of phase noise introduced by an optical fiber or other time-varying path.* Opt. Lett. **19** (21), 1777 (1994).

[17] D. Hume. *Two-Species Ion Arrays for Quantum Logic Spectroscopy and Entanglement Generation.* Ph.D. thesis, NIST (2010).

[18] G. Kirchmair. *Frequency stabilization of a Titanium-Sapphire laser for precision spectroscopy on Calcium ions.* Diploma thesis, Universität Innsbruck (2006).

[19] M. Sepiol. *Frequency stabilization of a 729 nm diode laser to an external high finesse reference cavity*. Master thesis, ETH Zürich (2012).

[20] C. Langer. *High Fidelity Quantum Information Processing with Trapped Ions*. Ph.D. thesis, NIST (2005).